



JGR Space Physics



RESEARCH ARTICLE

10.1029/2019JA027285

Key Points:

- We observe mesospheric clouds 18 s after releasing 220 kg of water at 85 km, that descend from 92 to 78 km, during winter in the Arctic
- The high water vapor concentrations (~1 ppv) enable cloud formation by both cooling the upper mesosphere and raising the frost point
- The cooling depends on the spatial distribution of the water vapor, with meter-scale pure water vapor filaments cooling most rapidly

Correspondence to:

R. L. Collins, rlcollins@alaska.edu

Citation:

Collins, R. L., Stevens, M. H., Azeem, I., Taylor, M. J., Larsen, M. F., Williams, B. P., et al. (2021). Cloud formation from a localized water release in the upper mesosphere: Indication of rapid cooling. *Journal of Geophysical Research: Space Physics*, 126, e2019JA027285. https://doi.org/10.1029/2019JA027285

Received 13 AUG 2019 Accepted 31 DEC 2020

© 2021. The Authors. This is an open access article under the terms of the Creative Commons Attribution NonCommercial License, which permits use, distribution and reproduction in any medium, provided the original work is properly cited and is not used for commercial purposes.

Cloud Formation From a Localized Water Release in the Upper Mesosphere: Indication of Rapid Cooling

Richard L. Collins¹, Michael H. Stevens², Irfan Azeem³, Michael J. Taylor⁴, Miguel F. Larsen⁵, Bifford P. Williams⁶, Jintai Li¹, Jennifer H. Alspach¹, Pierre-Dominique Pautet⁴, Yucheng Zhao⁴, and Xun Zhu⁷

¹Department of Atmospheric Sciences, Geophysical Institute, University of Alaska Fairbanks, Fairbanks, AK, USA, ²Space Science Division, Naval Research Laboratory, Washington, DC, USA, ³ASTRA LLC, Boulder, CO, USA, ⁴Department of Physics, Center for Atmospheric and Space Sciences, Utah State University, Logan, UT, USA, ⁵Department of Physics, Clemson University, Clemson, SC, USA, ⁶GATS, Boulder, CO, USA, ⁷Johns Hopkins University Applied Physics Laboratory, Laurel, MD, USA

Abstract Polar mesospheric clouds (PMCs) occur in the summer near 82-85 km altitude due to seasonal changes of temperature and humidity. However, water vapor and associated PMCs have also been observed associated with rocket exhaust. The effects of this rocket exhaust on the temperature of the upper mesosphere are not well understood. To investigate these effects, 220 kg of pure water was explosively released at 85 km as part of the Super Soaker sounding rocket experiment on the night of January 25–26, 2018 at Poker Flat Research Range (65°N, 147°W). A cloud formed within 18 s and was measured by a ground-based Rayleigh lidar. The peak altitude of the cloud appeared to descend from 92 to 78 km over 3 min. Temperatures leading up to the release were between 197 and 232 K, about 50 K above the summertime water frost point when PMCs typically occur. The apparent motion of the cloud is interpreted in terms of the expansion of the explosive release. Analysis using a water vapor radiative cooling code coupled to a microphysical model indicates that the cloud formed due to the combined effects of rapid radiative cooling (~25 K) by meter-scale filaments of nearly pure water vapor (~1 ppv) and an increase in the frost point temperature (from 150 to 200 K) due to the high concentration of water vapor. These results indicate that water exhaust not only acts as a reservoir for mesospheric cloud production but also actively cools the mesosphere to induce cloud formation.

Plain Language Summary The effects of water vapor exhaust from space traffic on the upper mesosphere is not well understood. Water can both contribute to cloudiness as well as cooling of the upper mesosphere. We released water from a rocket at 85 km to study these effects. We detected an ice cloud with a ground-based laser radar soon after the release. The rapid formation of the cloud indicates that space traffic water exhaust may not only provide water for production of clouds but also cool the mesosphere to induce the formation of these clouds.

1. Introduction

Polar mesospheric clouds (PMCs) appear in the Arctic or Antarctic summer near 82-85 km. They are composed of water ice particles and have been routinely observed by a wide variety of ground-based and satellite instruments (e.g., Russell et al., 2009 and references therein). PMCs typically form in the cold (<150 K) and dry (1 ppmv) conditions of the summer polar mesosphere (e.g., Rapp & Thomas, 2006; von Zahn & Berger, 2003). The clouds are highly sensitive to the ambient temperature and humidity of the upper mesosphere and are therefore diagnostic of both small- and large-scale variations in the local meteorological conditions. This makes them a compelling target to test our understanding of energetics and microphysics in the upper atmosphere. Studies have focused on both the natural occurrence of the clouds as well as their formation induced by rocket exhaust. Previous studies have shown the role of the National Aeronautics and Space Administration (NASA) Space Shuttle's main engine water exhaust in the formation of polar mesospheric cloud (PMC) in the Arctic and the Antarctic (Collins et al., 2009; Kelley et al., 2010; Stevens et al., 2003; Stevens, Englert et al., 2005a; Stevens, Meier et al., 2005b; Stevens et al., 2012). Case studies have shown that one burst of these space shuttle-generated PMCs can account for roughly 10%–20% of the total ice mass observed in one season of observations over the Arctic or the Antarctic (Stevens, Englert et al., 2005a;

COLLINS ET AL. 1 of 21



Stevens, Meier et al., 2005b). These bursts were primarily distinguished by an increase in PMC frequency, rather than brightness (DeLand & Thomas, 2019). However, neither the total contribution of space shuttle launches to the observed numbers of PMC nor the cumulative contribution of space traffic worldwide to the historical cloud record has yet been quantified.

The fate and transport of concentrated water plumes in the upper mesosphere-lower thermosphere (UMLT, \sim 80–100 km) region has attracted considerable attention (e.g., Kelley et al., 2010; Liu, 2007; Meier et al., 2010; Pumphrey et al., 2011; Siskind et al., 2013; Stevens et al., 2014; Yue et al., 2013). These plumes raise a number of important questions about UMLT processes, ranging from dynamics and chemistry to PMC formation and climatology. Our fundamental understanding of how these plumes undergo a phase change to ice clouds lacks maturity. To date, no study, either observational or numerical, has quantified the microphysics, energetics, and transport of a water plume in the UMLT and explored the implications for PMC formation and the thermodynamics of this region.

To our knowledge, the impact of water vapor infrared (IR) cooling on mesospheric cloud formation has yet to be constrained with observations. This is primarily because the upper mesosphere is typically so dry that the contribution of cooling to the thermal budget by the naturally occurring water vapor is relatively small (~1 ppmv). In this study, we describe a sounding rocket experiment that we designed and conducted to determine how concentrated water vapor (~1 ppv, representing pure water vapor) impacts the PMC formation environment in the upper mesosphere. In this experiment water was released in the Arctic polar mesosphere and resulted in the immediate formation of a mesospheric ice cloud. Our experiment was deliberately conducted under inhospitable conditions for PMC formation (January in the Arctic) to test how efficiently water vapor can locally cool the upper mesosphere. The experiment took place at Poker Flat Research Range (PFRR), Chatanika, Alaska (65°N, 147°W). A coordinated suite of ground-based instruments was operated at PFRR to observe the cloud as well as its environment before, during, and after the release. We extend a contemporary aerosol model and a radiation model to investigate the impact of this water release on the local temperature as well as the time-dependent microphysics leading to ice particle formation and sublimation. We find that the introduction of such concentrations of water vapor in a filamentary structure can quickly drive the temperature down to the water frost point that has been significantly increased $(\sim 50 \text{ K})$ by the elevated water vapor mixing ratio, even in the polar winter.

This study is organized as follows: Section 2 describes the experiment design as well as the participating ground-based instruments. Section 3 describes the temperature observations and the cloud observations. Section 4 presents our interpretation the geometry of the release and the shape of the cloud. Section 5 presents the coupled aerosol and radiation model used to interpret the observations, the results of the microphysical modeling, and the comparison with the observations. Section 6 discusses the results and their impact on our understanding of the PMC environment.

2. Experiment, Instruments, and Methods

2.1. The Super Soaker Rocket Experiment

On the night of January 25–26, 2018, a controlled water release experiment in the upper mesosphere was performed from PFRR. This experiment, called "Super Soaker", consisted of three sounding rockets; two rockets carrying trimethyl aluminum (TMA) tracers, and a third rocket carrying 220 kg of liquid water. The water release section was a 43.2 cm (17 inches) diameter and 152.4 cm (60 inches) long aluminum payload structure with black powder charges at each end. Each powder charge receptacle contained 0.7 kg (1.54 lb) of powder charge. The water release section consisted of two canisters conjoined by a sealed V-band. Internal baffles were included in the canister design to minimize fluid motion of the water during spin up of the payload. During the release, two V-band guns in the center of the section separated the canisters and simultaneous ignitions of the two powder charges dispersed the water.

The Super Soaker rocket salvo occurred between 0500 and 0600 Local Standard Time (LST = UT -9 h, 1400 and 1500 UT) on January 26, 2018 over a period of 40 min. The three sounding rockets were Terrier Improved Orion rockets (NASA code 41) and identified as 41.119, 41.120, and 41.122, respectively. The rocket trajectories, release point, and Rayleigh lidar beam are shown in Figure 1. The first two sounding

COLLINS ET AL. 2 of 21

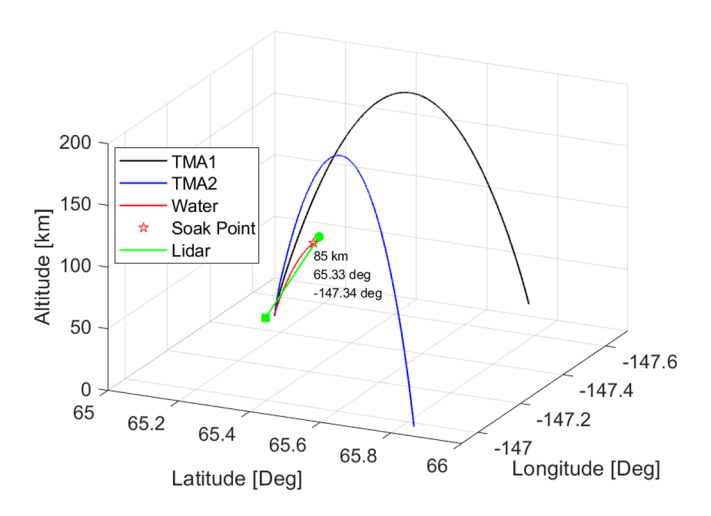


Figure 1. Trajectories of the three sounding rockets during the Super Soaker experiment. The black and blue solid lines show the trajectories of the two rockets carrying TMAcanisters. The red solid line shows the trajectory for the third rocket. The green solid line shows the Rayleigh lidar beam. The third rocket trajectory and Rayleigh lidar beam are only plotted up to the water release or soak point at 85 km altitude (85.33°E, 147.34°W). The lidar beam and release point are separated by 3.7 km at 85 km. TMA, trimethyl aluminum.

rockets, each carrying a TMA canister, were launched at 14:11:34 UT and 14:48:19 UT, respectively. The third and final rocket, carrying the water, was launched 90 s later at 14:49:49 UT. Upon reaching 85 km altitude 100.5 s after launch, the third rocket explosively released its water payload at 14:51:29 UT. A Rayleigh lidar was located at 65.11°N and 147.47°W and pointed toward the release point 24.5 km downrange. The water was explosively released at 85 km altitude at 14:51:29 UT. The trajectory shown for the rocket carrying water terminates at the point of explosion. The Rayleigh lidar beam shows the location of the lidar sensing volume relative to the water release point. At 85 km, the lidar beam was 3.7 km north east of the release point. The trajectories of the second and third rocket were well-separated in both space and time and did not overlap (Figures 1 and 2). The TMA trails from the first two rockets provide an estimate of the horizontal neutral wind response before and after the water release. The TMA trails revealed horizontal winds typical of quiet geomagnetic conditions (Mesquita et al., 2020). There was a strong eastward and northward jet with maximum winds of 80-100 m/s present between 93 and 100 km. The winds were less than 50 m/s below 90 km. There was no observable change in the horizontal winds directly attributable to the release of the water, and therefore we focus exclusively on the third rocket and the water release.

2.2. Rayleigh Lidar

A steerable Rayleigh lidar was developed to support the Super Soaker experiment. The Rayleigh lidar consisted of a Nd:YAG laser, a 0.78 m diameter f-3.7 Newtonian telescope, and a steerable 1.04 m mirror. The steerable mirror served to both direct the transmitted laser beam as well as reflect the laser light backscattered from the sky into the telescope (Li, 2019). The light collected by the telescope was fiber-coupled to the detection system. The detection system included an optical chopper, collimating optics, interference filter, photomultiplier tube, a photon counting data acquisition system, and computer. The laser operated at

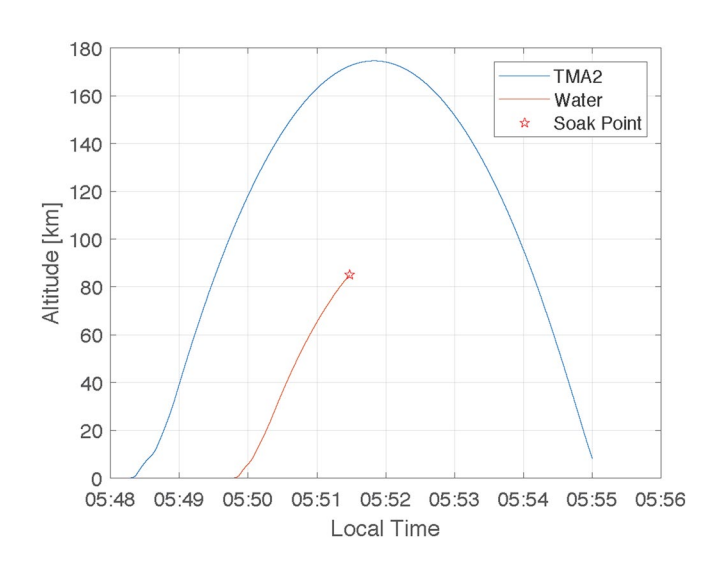


Figure 2. Flight paths of the second rocket carrying a TMA canister (blue) and the third rocket (red) carrying the water payload as a function of local time. The trajectory of the third rocket is plotted up to the release point at 85 km altitude where 220 kg of water was released at 05:51:29 local time (14:51:29 UT). TMA, trimethyl aluminum.

532 nm with a pulse repetition rate of 20 pps. The laser pulse width was 7 ns FWHM and the laser had an average power of 8.5 W. The field of view of the receiver was 1.7 mrad (defined by the fiber coupling lens) and the optical bandwidth was 0.3 nm FWHM. Lidar signals were acquired over $0.32~\mu s$ intervals, yielding a range resolution of 48 m. For the Super Soaker experiment the Rayleigh lidar beam was directed $10^{\circ}E$ of N and 18° off-vertical. The beam was 3.7~km from the release point at an altitude of 8.5~km

For the cloud observations, the raw data profile consists of the integration of the backscattered signal from 500 laser pulses over 25 s. We characterize the cloud by the standard PMC metrics: aerosol backscatter ratio; volume backscatter coefficient; and integrated backscatter coefficient (e.g., Collins et al., 2009). The aerosol backscatter coefficient is calculated from the lidar data in a two-step process. We first determine the molecular density profile based on the lidar measurements preceding the rocket launch. We then determine the aerosol backscatter ratio by normalizing the profiles with clouds to the lidar profiles without clouds preceding the release. We then determine the backscatter coefficient from the backscatter ratio using the molecular concentration from the Mass Spectrometer Incoherent Scatter (MSIS) model and the Rayleigh molecular back scattering cross section for dry air (Hedin, 1991; Measures, 1992). We characterize the cloud altitude and width based on the backscatter coefficient profile.

COLLINS ET AL. 3 of 21

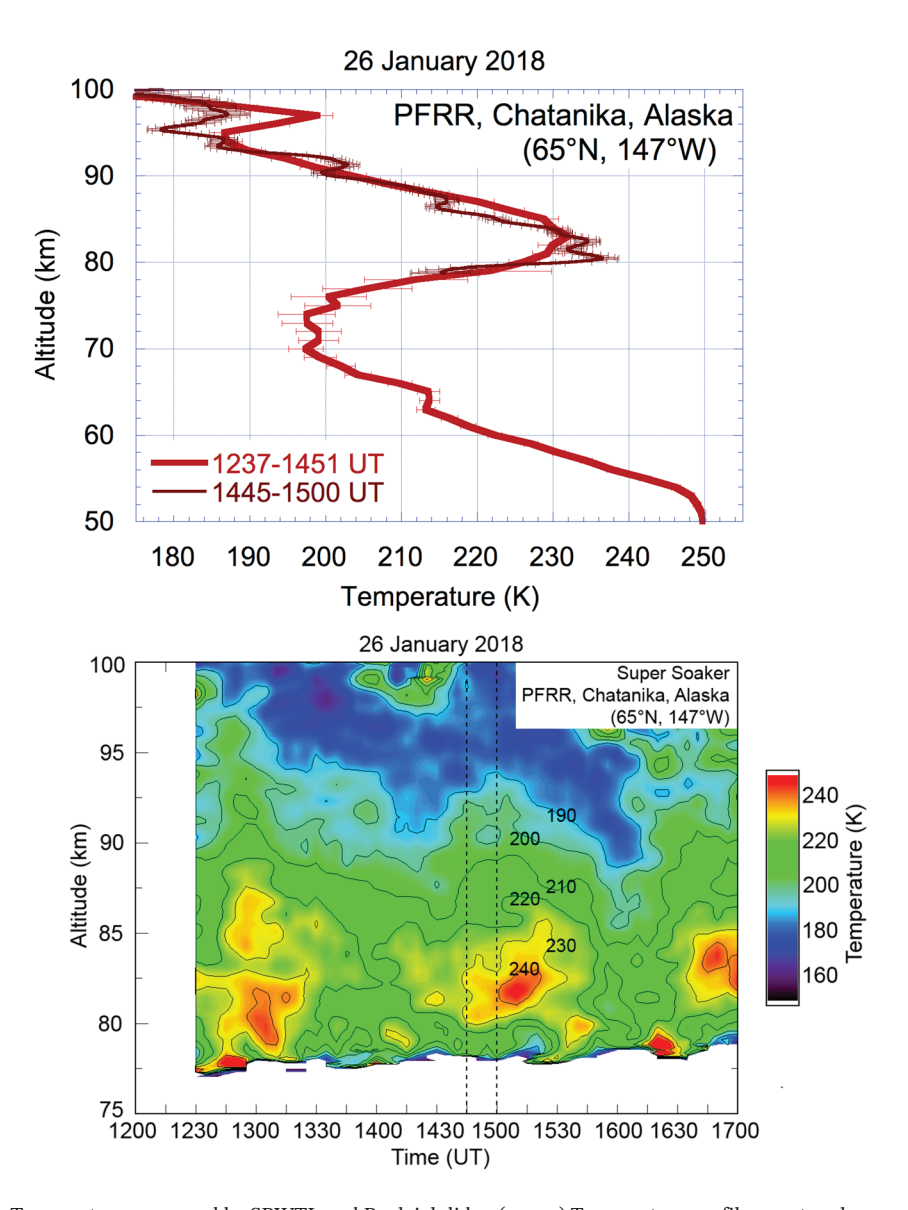


Figure 3. Temperature measured by SRWTL and Rayleigh lidar. (upper) Temperature profile over two-hour period preceding and over the 15 min spanning the Super Soaker launch. The error bars represent the one-sigma uncertainties in the temperatures (lower) Temperature plotted as a function of altitude and time (150 K, 250 K) integrated over 15 min at 5 min intervals. Contours are plotted at 10 K intervals from 190 to 240 K. The dashed lines are at 1445 and 1500 UT spanning the launch (see text for details). SRWTL, sodium resonance wind-temperature lidar.

The Rayleigh lidar observations also yield measurements of temperature preceding the rocket launch when the lidar signal is dominated by scattering from molecules with negligible scattering from aerosols. For the temperature observations, the raw data profile consists of the integration of the backscattered signal from 1,000 laser pulses over 100 s. The temperature profile is derived using established techniques from the density profile measured by the lidar under the assumption of hydrostatic equilibrium and an initial temperature at the upper altitude of the profile near 80 km (e.g., Collins et al, 2011). The systematic uncertainty due to the initial temperature is removed by using an initial temperature provided by a collocated sodium resonance wind-temperature lidar (SRWTL, described in the next section). The Rayleigh temperature profile is determined over the 40–80 km altitude region (Figure 3). The statistical uncertainties in the temperature are less than 0.1 K at 40 km and increases to 8 K at 79 km for a temperature profile with an integration period of 2 h. The choice of a 2-h interval preceding the launch ensures sufficient signal to yield

COLLINS ET AL. 4 of 21



small statistical errors as well as avoid any biases due to contributions to the lidar signal from the products of the Super Soaker release.

2.3. Sodium Resonance Wind-Temperature Lidar

An SRWTL was deployed and upgraded to support the Super Soaker experiment (Li et al., 2020). The SRWTL used the three-frequency technique to measure wind and temperature in the mesospheric sodium layer (\sim 80–100 km; Bills et al., 1991; Krueger et al., 2015; She et al., 1990). The SRWTL was located \sim 10 m from the Rayleigh lidar. The SRWTL was directed in the vertical and the beam is 27.6 km from the Rayleigh beam and was 24.5 km from the release point at an altitude of 85 km. The SRWTL observations are acquired at a raw resolution of 5 s and 48 m in the vertical. These observations yield temperature measurements over the altitude range of the sodium layer (\sim 80–100 km) at a resolution of 15 min and 1 km with statistical and systematic uncertainties of less than 2 K (Figure 3).

2.4. Advanced Mesospheric Temperature Mapper

The Advanced Mesospheric Temperature Mapper (AMTM) is an IR digital imaging system that measures the intensity and temperature of the hydroxyl (OH) emission layer that spans the water release altitude of 85 km (Pautet et al., 2014). The AMTM utilizes a fast telecentric lens system and a cooled InGaAs array to observe structure in the OH (3,1) band at \sim 1.55 μ m that yields measurements of gravity waves with periods ranging from several minutes to several hours and associated temperature structure (e.g., Cai et al., 2014; Heale et al., 2017; Pautet et al., 2018; Yuan et al., 2016).

For the Super Soaker experiment, a 120° field-of-view AMTM was installed and operated at PFRR. The AMTM was located 1.6 km away from the lidars. The AMTM sequentially measured the $P_1(2)$ and $P_1(4)$ emission lines of the OH (3,1) band and a nearby spectral background. OH rotational temperature maps were determined using the line-pair-ratio method (Meriwether et al., 1975). The method has been adapted for the OH (3,1) band (Pautet et al., 2014). For routine nighttime measurements at PFRR, a cyclic exposure time of 10 s/filter was used resulting in a time series of band intensity and temperature maps on uniform grids (\sim 200 \times 160 km), every \sim 30 s, with a zenith spatial resolution of \sim 0.625 km/pixel. For several test nights and for the Super Soaker mission night, a reduced exposure time of 4 s/filter was used to yield maps at an increased resolution of 12–15 s while maintaining a high temperature precision (\sim 2–3 K/pixel). The AMTM has previously been cross-calibrated using observations alongside an SRWTL yielding an accuracy of \sim 5 K (Yuan et al., 2014).

3. Observations

3.1. Temperature

Immediately preceeding the Super Soaker rocket launches, the temperature profile shows a stratopause with a temperature maximum of 250 K at 50 km and a secondary maximum of 232 K at 83 km (Figure 3, upper panel). The temperature profile is a composite of the measurements with the Rayleigh lidar temperatures between 40 and 79 km averaged from 12:37-14:52 UT and the SRWTL between 80 and 100 km averaged from 12:35-14:52 UT. The SRWTL temperature profile over 15 min spanning the launch (1445-1500 UT) shows similar structure as the 2-h profile with wave fluctuations with a vertical wavelength of about 5 km superimposed on the background profile indicative of gravity wave activity that is commonly observed in the UMLT (e.g., Chen et al., 2016; Chu et al., 2011). The temperatures are greater than 198 K over the 80-90 km altitude region. The SRWTL and AMTM temperature measurement both show a pronounced 2-h variation (Figure 3, lower panel Figure 4, upper panel). The Sounding of the Atmosphere using Broadband Emission Radiometry (SABER) instrument onboard the Thermosphere Ionosphere Mesosphere Energetics Dynamics (TIMED) satellite makes measurements of the OH Meinel airglow layer (e.g., Marsh et al., 2006). TIMED-SABER reported the OH layer peak at 83 km at (62.4°N, 147.6°W) at 15:35 UT. The AMTM and the SRWTL (Gaussian weighted average SRWTL temperature measurements centered at 83 km with a 7 km FWHM) report temperatures of 225 K at the release and local maxima of 230 K following the water release (Figure 4, upper and lower panels). The AMTM measurements represent a spatial average

COLLINS ET AL. 5 of 21

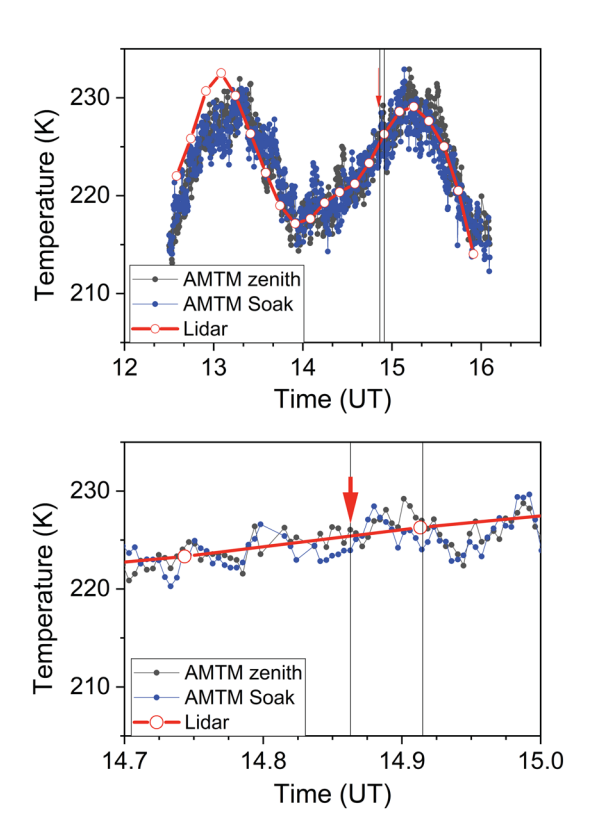


Figure 4. Temperature measured by SRWTL (red) and AMTM (blue and black). The AMTM measurements are based on the measurements in the vertical (blue) and at the release or "soak" point (black). The red arrow indicates the time of the water release. The vertical lines span the period when the cloud was detected by the Rayleigh lidar. See text for details. AMTM, Advanced Mesospheric Temperature Mapper; SRWTL, sodium resonance wind-temperature lidar.

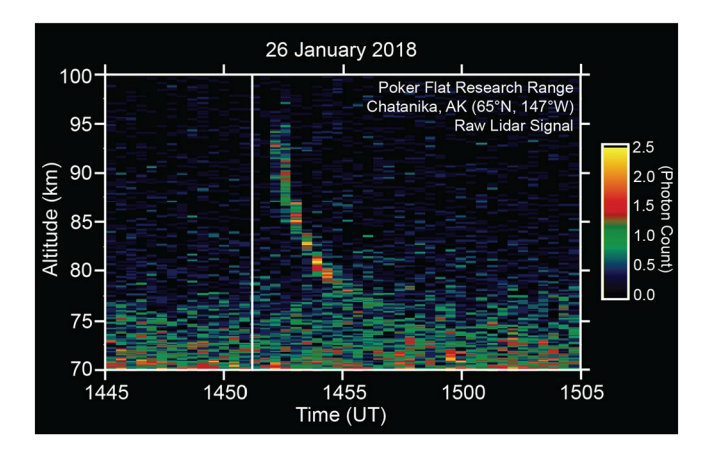


Figure 5. Raw Rayleigh lidar signal from artificial cloud released over PFRR on January 26, 2018 plotted as a function of time and altitude. The raw signal is acquired at 48 m in range (45.7 m in altitude) and 25 s resolution in time. The signal is smoothed with a five-point running average in range. The cloud is clearly visible between 14:52 and 14:55 UT and 92 and 78 km. The vertical white line marks the time of the water release. The signal below 77 km represents the Rayleigh scatter from the atmosphere which increases with decreasing altitude.

over 2 km \times 2 km (corresponding to a three pixel by three-pixel average) around the zenith and around the release point, while the SRWTL measurements are in the vertical above PFRR. The SRWTL and AMTM temperature measurements differ by less than 2 K, validating the initial temperatures used in our simulation of the water release to within 2 K.

3.2. Mesospheric Cloud

The Rayleigh lidar detects enhanced backscattering in the upper mesosphere between 14:52 and 14:55 UT in a sequence of eight lidar profiles (Figure 5). The enhanced backscattering appears \sim 18 s after the rocket water release near 92 km, based on the middle of the lidar integration timestep as the point of reference (14:51:35 + 12.5 s). The backscatter coefficient profiles initially show a peak backscatter ratio of 35 with a backscatter coefficient of 8.5×10^{-11} m $^{-1}$ sr $^{-1}$ at 92.2 km and a FWHM of 4.6 km (Figure 6). The peak then appears to descend over time to an altitude of 78.1 km before disappearing (Figure 7). The observed peak initially descends with an apparent velocity of 127 m/s (14:52–14:53) and then descends less rapidly at 31 m/s (14:54–14:55). The observed FWHM of the ice cloud varies between 6.3 and 2.3 km. The peak backscatter ratios, backscatter coefficients, and corresponding altitudes are tabulated in Table 1.

The peak backscatter ratio varies between 2 and 35 with an average value of 14. The peak backscatter coefficient varies between $4.6 \times 10^{-11} \, \mathrm{m}^{-1} \, \mathrm{sr}^{-1}$ and $1.7 \times 10^{-10} \,\mathrm{m^{-1} \, sr^{-1}}$ with an average value of $1.1 \times 10^{-10} \,\mathrm{m^{-1} \, sr^{-1}}$. The cloud has a maximum peak backscatter coefficient of $1.7 \times 10^{-10} \,\mathrm{m}^{-1} \,\mathrm{sr}^{-1}$ at 80.4 km with a peak backscatter ratio of 11. The ratio of the integrated backscatter ratio to the integrated molecular backscatter ratio varies between 1 and 35 with an average value of 11. The integrated aerosol backscatter coefficient is calculated over the FWHM of the cloud and varies between $1 \times 10^{-7} \, \mathrm{sr}^{-1}$ and $7 \times 10^{-7} \, \mathrm{sr}^{-1}$ with an average value of 3×10^{-7} sr⁻¹. The cloud is an order of magnitude optically thinner than PMCs that have been reported from lidar measurements in the Arctic (e.g., Collins et al., 2009; Fiedler et al., 2003). As regards the evolution of the cloud over the eight profiles, the peak backscatter coefficient of the cloud remains relatively constant between the second and sixth profiles. The integrated backscatter coefficient is largest when the cloud FWHM is a maximum of 6.3 km in the second profile, and remains relatively constant between the third and sixth profiles when the FWHM is between 2.3 and 3.2 km.

Microphysical cloud properties can be derived from the lidar measurements under the assumption that the cloud is composed of spherical water ice particles of a given radius (Bohren & Huffman, 1983; Flatau, 2018). For the peak backscatter ratio of $1.7\times10^{-10}~\text{m}^{-1}~\text{sr}^{-1}$ at 80.4 km, the corresponding particle densities are $6.5\times10^5~\text{m}^{-3}$ and the corresponding ice mass density is $2.6\times10^{-12}~\text{kg/m}^3$ for 100 nm radius particles. We do not have direct ice particle size observations and this size is based on the typical particle size observed and modeled in the polar mesosphere (e.g., Rapp & Thomas, 2006; von Savigny & Burrows, 2007).

4. Interpretation of Observations

4.1. Motivation

The Super Soaker cloud observations present two challenges. The first challenge is the rapid appearance of the clouds 18 s after the release of

COLLINS ET AL. 6 of 21

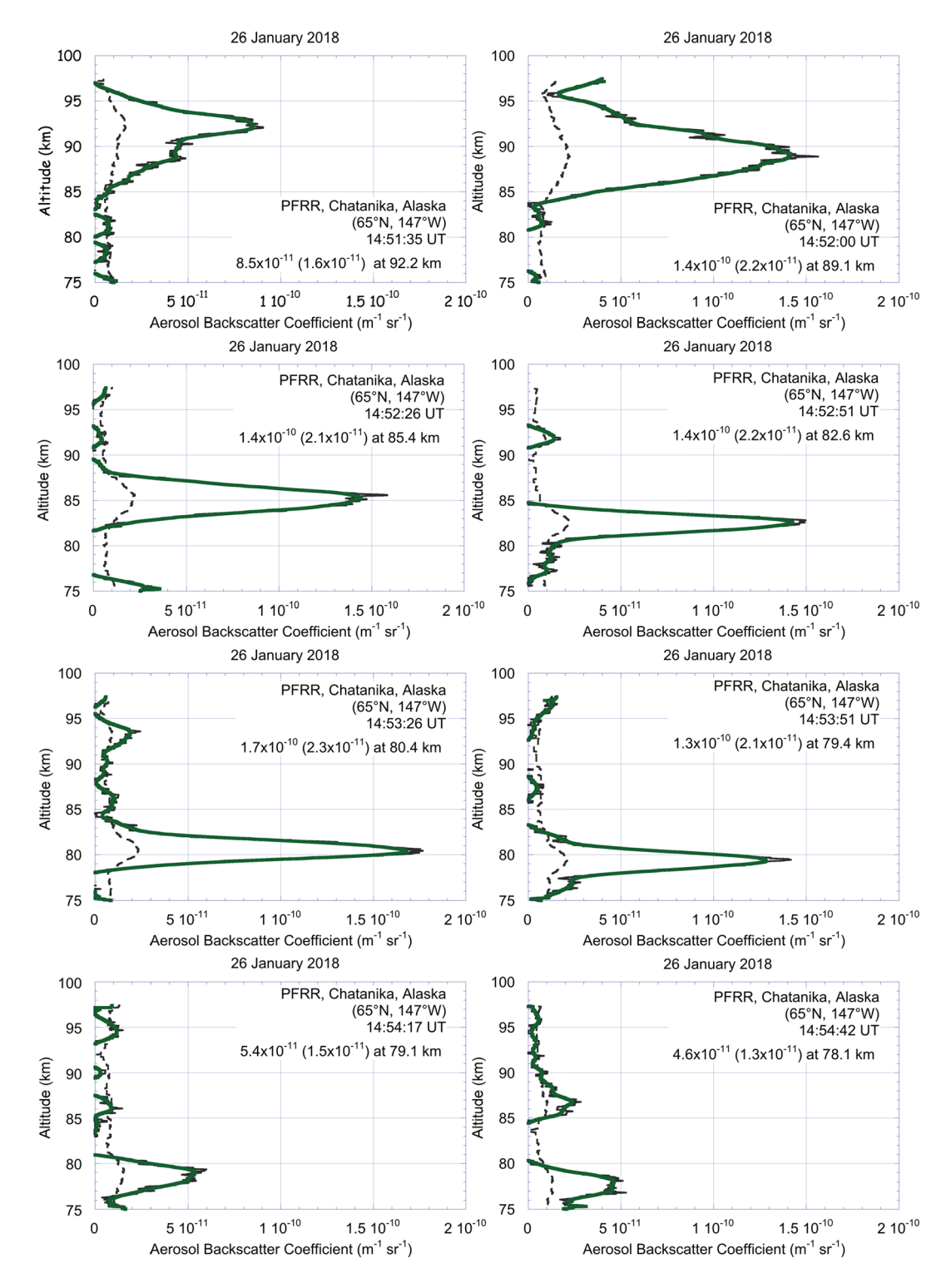


Figure 6. Aerosol backscatter coefficient profiles derived from Rayleigh lidar measurements plotted as a function of altitude. The thin solid black curves represent the backscatter coefficient derived from the lidar signal that has been smoothed by 2 km. The thin broken black curves represent the uncertainty in the backscatter coefficient based on statistical uncertainty in the lidar signal. The green curve represents the backscatter coefficient profile smoothed with a 1 km running average. The peak backscatter coefficient, altitude and uncertainty (in parenthesis) are listed on each plot.

COLLINS ET AL. 7 of 21

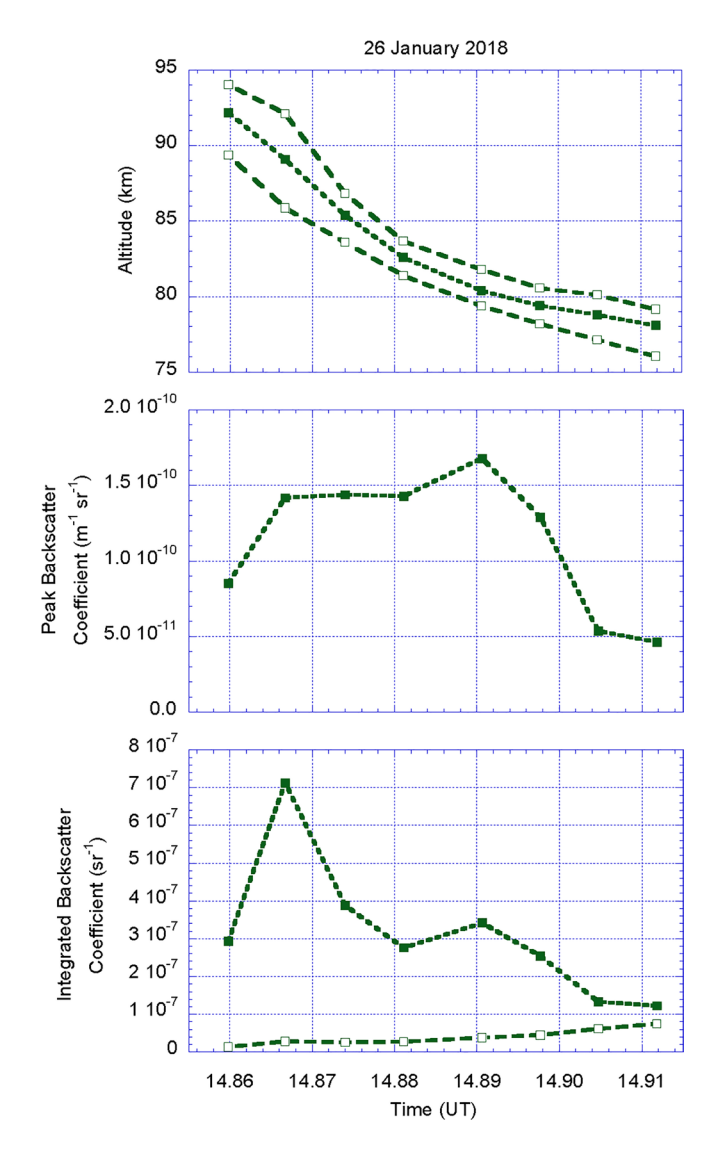


Figure 7. Properties of artificial cloud released at PFRR on January 26 plotted as a function of time. Upper: Altitude of peak (green short dash with closed square) and altitude of half-maximum (green long dash with open square). Middle: Peak backscatter coefficient. Lower: Integrated aerosol backscatter coefficient over FWHM of cloud (green short dash with closed square) and integrated molecular backscatter coefficient over FWHM (green long dash with open circle). PFRR, Poker Flat Research Range.

the water. Mesospheric clouds almost never form outside the summer season (e.g., Gadsden, 1982; Warren et al., 1997). During polar summer such clouds typically exist at temperatures below 150 K (e.g., Jensen & Thomas, 1988), which is over 50 K lower than the temperature measured by the lidars (Figures 3 and 4). The second challenge is the rapid descent of the cloud peak with an apparent vertical velocity of 31-127~m/s (Figure 7), as vertical winds in the UMLT are typically less than 1 m/s (e.g., Berger & von Zahn, 2002).

While the frost point for water vapor mixing ratios of a few ppmv typical of the polar summer mesosphere is ~150 K, the frost point for the more humid conditions of 1 ppv associated with the Super Soaker experiment is ~200 K (Figure 8, Marti & Mauersberger, 1993; Stevens et al., 2002). The temperature profiles measured by the lidars show that under these extremely humid conditions ice can form above 91 km and below 78 km, but requires a temperature decrease of ~25 K to form between 80 and 85 km. Thus, we consider the possibility that the Super Soaker cloud is formed by an expanding shell of water vapor that rapidly cools the upper mesosphere and drives temperatures down to the elevated water frost point. Ambient water vapor mixing ratios at 85 km are typically a few ppmv or less, leading to IR cooling rates of about 1 K/day (Fomichev et al., 2004), which are small compared to other calculated heating rates of about 10 K/day in the polar summer mesosphere (Thomas, 1996; Zhu, 1994). However, we will show that large amounts of water vapor (1 ppv) in a filamentary structure can produce local cooling rates of about 1 K/s. This cooling can drive the temperature down to the frost point in seconds, thereby allowing mesospheric water ice cloud formation in the polar winter mesosphere.

4.2. The Nature and Geometry of the Cloud

The Super Soaker payload of 220 kg of water was kept warm enough to remain in liquid form on the launch pad and during its ascent. We consider four possible sources of the enhanced backscattering observed by the Rayleigh lidar in the upper mesosphere: liquid water from the payload; debris from the exploding payload; debris from ignition of a rocket stage; and ice clouds from the released water. We expect that the water evaporates when it is explosively released at the ambient pressure of ~0.3 Pa at 85 km. Two experiments using the Saturn launch vehicle in the 1960s provide insight into the fate of water released in the upper atmosphere (Woodbridge et al., 1963; Woodbridge & Lasater, 1965). The "High Water" experiments consisted of two releases of water in the thermosphere and associated laboratory experiments (Woodbridge et al., 1963; Woodbridge & Lasater, 1965).

In the High Water releases 42–44 tonnes of water were explosively released at 105 and 165 km. Clouds formed in less than a second after the water was released. In the High Water laboratory experiments 3 cm 3 of water was released into a volume of 3×10^7 cm 3 at a pressure of 2×10^{-4} mbar (typical of atmosphere near 89 km). The released water changed into the ice phase less than 10 ms after the release (Woodbridge et al., 1963). Since this is much less than the time we observe the cloud after the Super Soaker release (18 s, Figure 7), we conclude that liquid water is not observed by the lidar in the Super Soaker experiment.

To determine whether the cloud is formed by rocket debris we consider the sedimentation speed v_s for a spherical particle of radius r in the upper mesosphere. This sedimentation speed is given by

COLLINS ET AL. 8 of 21

Table 1Peak Aerosol Backscatter Ratio and Backscatter Coefficient

Time (UT) ^a	Altitude (km)	Aerosol backscatter ratio	Altitude (km)	Backscatter coefficient $(\times 10^{-11} \text{ m}^{-1} \text{ sr}^{-1})$
14:51:35	92.2	35 ± 7	92.2	8.5 ± 1.6
14:52:00	89.9	35 ± 6	89.1	14 ± 2.2
14:52:26	85.6	19 ± 3	85.4	14 ± 2.1
14:52:51	82.8	13 ± 2	82.6	14 ± 2.2
14:53:26	80.6	11 ± 2	80.4	17 ± 2.3
14:53:51	79.5	7.1 ± 1	79.4	13 ± 2.1
14:54:17	79.2	2.8 ± 1	79.1	5.3 ± 1.5
14:54:42	78.3	2.1 ± 1	78.1	4.6 ± 1.2

 $^{\mathrm{a}}$ The time is recorded at start of each profile acquisition. Each profile is derived from 25 s of signal integration and each observation has a vertical resolution of 48 m.

$$v_s = \frac{\rho g r}{2n} \times \left(\frac{\pi}{2m_a k T}\right)^{1/2} \tag{1}$$

where g is the acceleration due to gravity, k is Boltzmann's constant, T is the temperature, m_a is the mass of a typical air molecule, n is the particle number density, ρ is the density of the particle material, and r is the particle radius (Reid, 1975). At 85 km the temperature was 229 K just prior to the release of the water so that Equation 1 reduces to

$$v_s \left(85 \,\mathrm{km} \right) = 2.8 \times 10^6 \times \rho \times r \tag{2}$$

where v_s is in cm/s, ρ is in g/cm³ and r is in cm. The density of water ice is 0.93 g/cm³ whereas the rocket is primarily composed of aluminum, which has a density of 2.7 g/cm³. Studies of high intensity explosions and collisions of orbital debris report representative fragment sizes of between 200 μ m and 1 cm (Zhang et al., 1997). Using the lower value of 200 μ m yields a fall speed of the aluminum debris of greater than 1.5 km/s, which is even larger than the 0.6 km/s vertical velocity of the

Super Soaker rocket at the time of the release and would fall out of our region of observations before the first detection of the cloud by the lidar. The aluminum debris would have to be an order of magnitude smaller ($<20~\mu m$) to yield fall speeds consistent with the apparent descent of the cloud (30–100~m/s). The possibility of such fine particles is not completely ruled out but is unlikely to be the case. We conclude that the cloud observed by the lidar is not metal debris from the rocket payload.

Four clouds in the mesosphere have been reported after the ignition of the fourth stage of Black Brant X and XII rockets above 85 km (Fricke et al., 1996; Thurairajah, 2009). These clouds were detected serendipitously by zenith pointing lidars located $\sim 30-50$ km from the rocket ignition. The clouds were detected 12–90 min after the ignition for periods of 15–70 min at altitudes of about 10 km below the ignition altitude between 65 and 90 km. However, the Terrier Improved Orion used in the Super Soaker experiment is a two-stage rocket where the second stage ignition is complete by the time the rocket reaches an altitude of 35 km. Thus we conclude that the cloud is not formed by exhaust products from the ignition of a rocket stage.

The rapid vertical motion of the cloud, descending approximately 14 km in 3 min (Figures 6 and 7) with apparent velocities of between 100 and 30 m/s, is much greater than the sedimentation speed of typical PMC particles. Typical 100 nm PMC particles have sedimentation speeds of approximately 0.3 m/s and would fall less than 0.05 km in this time. The ice particles would have to have radii of $10-30~\mu m$ to sediment this rapidly. Based on the measured lidar backscatter coefficients such large particles would be very sparse (<0.1 m⁻³). Given the concentration of dust particles serving as nucleation sites (> $10^7~m^{-3}$, Wilms et al., 2016) we expect that the cloud is formed of a larger number of smaller particles typical of PMC. We conclude that the rapid descent of the cloud does not represent the sedimentation of large ice particles.

We suggest that the evolution of the cloud as measured by the Rayleigh lidar is consistent with the expansion of a spherical shell of water ice following the explosive water release (Figure 9). We assume that the center of the shell travels upward due to the vertical velocity of the rocket and expands with a radial velocity due to the explosive release. At a distance of 3.7 km from the release point, the 220 kg of water would create a spherical shell that is 1.35 m thick with a water concentration of 1 ppv. The initial appearance of the cloud near 92 km with the largest FWHM (6.3 km) reflects the passage of the leading edge of the shell through the lidar beam. As the shell continues to expand, the lower edge of the shell travels across the lidar beam and the cloud appears to descend less rapidly with a smaller FWHM (2.3–3.2 km). The relative constancy of the peak backscatter coefficient is consistent with a uniform shell. The variation of the integrated backscatter coefficient is also consistent with the expansion of a uniform shell where the values are greatest when the FWHM is largest coinciding with the passage of the leading edge of the shell.

We estimate the velocities associated with the shell based on the following observations: the vertical velocity of the rocket at the time of release was 553 m/s; the appearance of the cloud at an altitude 7.2 km

COLLINS ET AL. 9 of 21

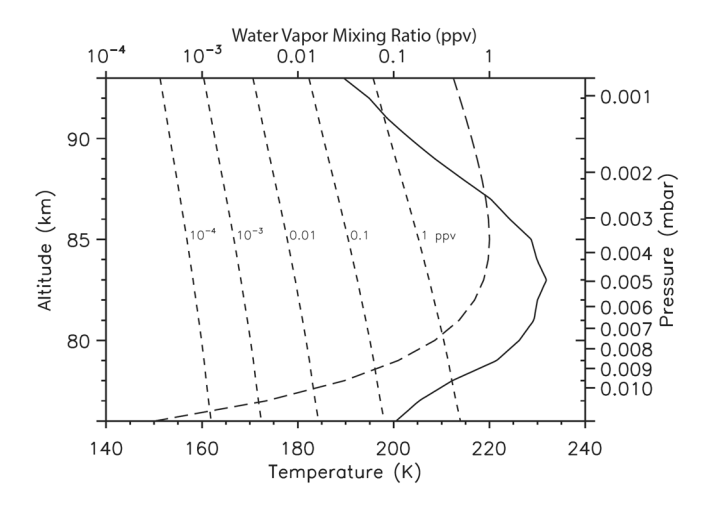


Figure 8. The water frost point as a function of temperature and altitude for a variety of water vapor mixing ratios relevant to this study (Marti & Mauersberger, 1993; dashed lines). The measured temperature profile immediately prior to the release of water (solid line, Figure 3) and the assumed water vapor mixing ratio profile of the release (long dashed line, Equation 3) are also plotted.

above the release point 18 s after the release; the appearance of the cloud 3.7 km from the release point, 18 s after the release; and the appearance of the cloud at 78 km, 924 s after the release. We expect that the velocity of the shell decreases in time due to atmospheric drag. The vertical motion is consistent with an initial vertical speed of 553 m/s that decreases exponentially with a decay time of 26 s and yields an average velocity of 400 m/s over 18 s. The horizontal motion and downward movement of the cloud is consistent with an initial explosive speed of 215 m/s that decreases exponentially with a decay time of 208 s and yields an average expansion speed of 206 m/s over the initial 18 s and an eventual net downward motion of the cloud. We conducted a ground test of the explosive release and determined the velocity of the water released to be 140 m/s from the video recording of the release. The explosive energy of the release determines its velocity. The explosive energy of 1.4 kg of black powder is 6 MJ (e.g., Akhavan, 1998). If this explosive energy was entirely converted into kinetic energy, the 220 kg of water would have a velocity of 230 m/s. While some explosive energy would be lost in rupturing the water cylinders, yielding a smaller explosive velocity for the water, we expect that the explosive velocity under near vacuum at 85 km would be larger than at the surface pressure on the ground. Finally, we expect that the expanding shell was deformed by the background winds (Mesquita et al., 2020). There were significant wind shears above 90 km where zonal and meridional jets had maximum wind speeds of 100 m/s and so the spherical shell would be significantly distorted above 90 km.

5. Microphysical Modeling of the Cloud

Our modeling of the cloud is guided by two observations of PMCs. First is that the lower edge of naturally occurring PMCs are found at temperatures that are remarkably repeatable of 150 K near 82 km which is close to the frost point (Lübken et al., 1996). Second is that recent balloon-borne imager observations have revealed filamentary structures as small as 30 m in PMCs (Fritts et al., 2017).

5.1. The Community Aerosol and Radiation Model for Atmospheres

We use the Community Aerosol and Radiation Model for Atmospheres (CARMA) to explore the interplay between the water vapor cooling and the ice particle heating, determine the thermal environment, and characterize the cloud. CARMA is a one-dimensional model of cloud microphysics. The model calculates nucleation, growth, sublimation, and sedimentation rates of ice particles and their resultant particle size distribution based on input profiles of temperature, pressure, water vapor, vertical winds, and nucleation sites (Rapp & Thomas, 2006). For this study, we use an updated version of CARMA (Wilms et al., 2016). Furthermore, our simulation is done in the rest frame of the expanding cloud of water. We make several modifications to the model to accommodate the rapid formation of the clouds, the small spatial scales, and the large quantity of water present in the Super Soaker experiment. These modifications are as follows:

- (a) The altitude resolution was reduced from 250 to 5 m, to better match the 48 m vertical resolution of the Rayleigh lidar cloud observations and model the radiative cooling of water vapor at high vertical resolution. For the standard CARMA model domain of 72–102 km, this yields a total of 6,000 altitude levels
- (b) The time step is reduced from 100 to 1 s to capture the evolution of the local temperatures from the time of the water release to the time of the first cloud observation 18 s later. The model is run over 432 time steps (7.2 min) in order to include the 3-min time period over which the clouds were observed
- (c) The background densities are taken from the NRL MSIS empirical model for January at latitude 65.1°N, longitude 212.6°E, and time 14:51 UT of our experiment (Picone et al., 2002)
- (d) The initial temperatures are taken from the temperature profile measured by the Rayleigh lidar and SRWTL (Figure 3)

COLLINS ET AL. 10 of 21

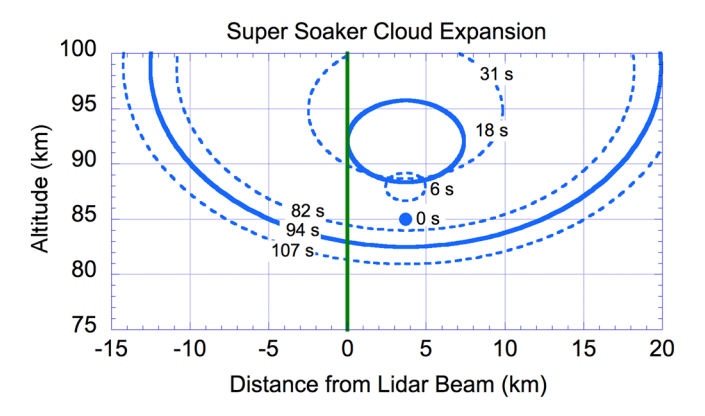


Figure 9. Schematic of expansion of Super Soaker water release relative to Rayleigh lidar beam. The release occurs at an altitude of 85 and 3.7 km from the lidar beam (green solid line). The explosive release is at 0 s. The location of the cloud is plotted at 6, 18, and 31 s after the release corresponding to the beginning (blue dashed), middle (blue solid), and end (blue dashed) of the first lidar profile (Figure 6). The location of the of the cloud is plotted at 82, 94, and 107 s after the release corresponding to the beginning, middle, and end of the fourth lidar profile (Figure 6). See text for details.

- (e) The initial background water vapor profile prior to the Super Soaker water release is taken from a simulation for the conditions of our experiment (latitude and day of year) using the National Center for Atmospheric Research (NCAR) Thermosphere Ionosphere Mesosphere Electrodynamics General Circulation Model (TIME-GCM; Roble & Ridley, 1994). We use a background water vapor profile with mixing ratios less than 0.1 ppmv throughout the region of interest. This is more than an order of magnitude less than water vapor mixing ratios typically found in the polar summer (e.g., Rapp & Thomas, 2006) and seven orders of magnitude less than those following the water release. We will discuss the simulated vertical distribution of the water release (1 ppv) in the next section
- (f) The initial vertical winds are taken from the TIME-GCM. These winds are less than 4 cm/s throughout the CARMA model domain and not enough to substantially affect the cloud development over the relatively short time period of our simulation. Eddy diffusion was set to zero at all altitudes
- (g) The vertical distribution of dust serving as nucleation sites is the same as that used in a recent study of realistic PMC formation (Wilms et al., 2016). The concentration of nucleation sites is less than that used in earlier CARMA studies (Rapp & Thomas, 2006)
- (h) A radiative cooling model (Zhu, 1994) is coupled into the CARMA framework and the water vapor cooling is calculated for each 1-s time step. We reduce the computation time by limiting our calculations to only those altitudes for which the water vapor mixing ratio is 10³ ppmv (0.001 ppv) or greater. Mixing ratios smaller than this do not significantly affect the temperature within the time period of our simulation. The radiative cooling model calculates the water vapor IR cooling rate by rotational lines and 6.3 micron vibrational-rotational band by use of the escape-to-space probability derived from the correlated k-distribution functions. The non-LTE processes for the 6.3 micron vibrational-rotational band are parameterized by an equivalent two-level model (Houghton, 2002; Zhu, 2004)
- (i) The release of latent heat associated with phase changes is calculated for each altitude and each timestep, and included in the time-dependent evolution of the temperatures
- (j) The parameterization of Siskind et al. (2007) is used to describe the infrared heating from ice particles and also included in the time-dependent evolution of the temperatures

The combination of the cooling (h) and the heating (i) and (j) is used to determine the temperature changes induced by the water release and cloud formation at each timestep. The temperature is updated at the end of the time step and the growth or sublimation of any ice particles is then recalculated with the updated temperature profile.

5.2. Modeling of Water and Cloud Formation

Once the water has evaporated, we expect radiative cooling in the gas phase to drive the local temperature to the elevated frost point. In this way, the released water passes through three phases (liquid to vapor to solid) in a period of less than a minute. Before incorporating a radiative cooling model into our ice formation model, we explore the impact of concentrated filaments of water vapor in on the local thermodynamics in the upper mesosphere.

We determine the cooling rates of layers, or filaments, of water vapor rate as a function of its mixing ratio for a variety of different widths from $0.1\,\mathrm{m}$ to $10\,\mathrm{km}$ (Figure 10). For narrow filaments $(0.1\text{--}1\,\mathrm{m})$, the cooling rate increases linearly with the water vapor mixing ratio. However, for broader filaments $(1\text{--}10\,\mathrm{km})$ the cooling rate is nonlinear due to increasing optical thickness that prevents the IR radiation from escaping to space. This nonlinearity is largest when mixing ratios are highest and the filaments are the broadest. The cooling is therefore fastest when the water is concentrated and distributed in the narrowest filaments. Cooling rates of $2.6\,\mathrm{K/s}$ can be reached for 1-m filaments of pure water vapor $(1\,\mathrm{ppv})$, which is fast enough to form ice particles within the time frame of our observations.

COLLINS ET AL. 11 of 21

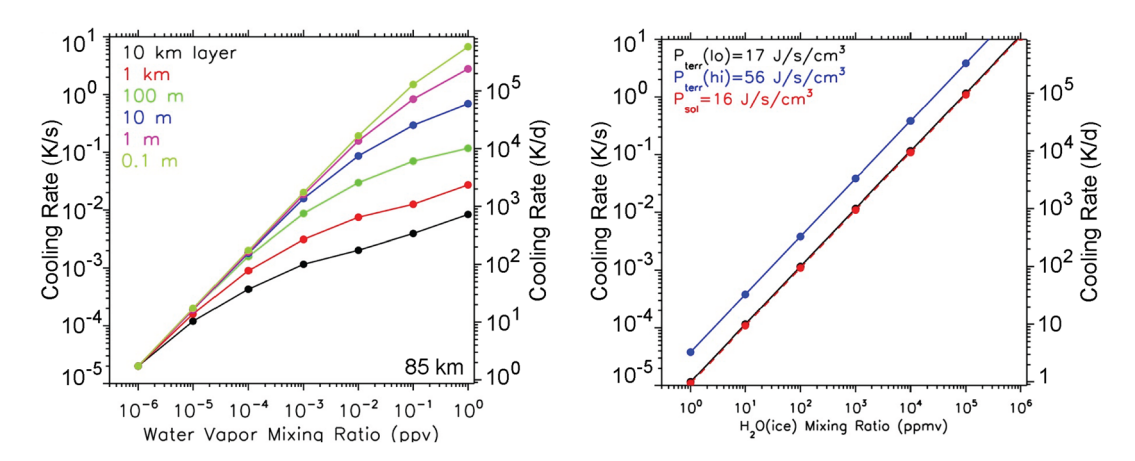


Figure 10. Left: Calculated water vapor cooling rates as a function of water vapor mixing ratio at 85 km altitude. Broader layers of water vapor cool less efficiently than narrower layers. Right: Calculated water ice heating rates as a function of equivalent water ice mixing ratio (μ_{ice}). The black line (17 W/cm³) and the blue line (56 W/cm³) represent a range of possible terrestrial heating rates (Siskind et al., 2007).

We characterize the initial water vapor mixing ratio distribution in terms of an initial peak mixing ratio vertical profile following the release and a length scale that describes the filamentary structure. The filaments are the result of the explosive release, and are described as Gaussian functions, that do not interact with each other. Since the payload is pure water vapor and we observe clouds approximately 5 km above and below the altitude of release, we adopt a smooth function centered at 85 km with a width of a few km to represent the water vapor distribution in the filaments immediately after its release. We choose a Chapman layer with a water vapor mixing ratio altitude profile f(z) that is defined by

$$f(z) = f_0 \exp\left(0.5 \times \left(1 - \left[\frac{z - z_0}{H_0}\right] - \exp\left[-\frac{z - z_0}{H_0}\right]\right)\right)$$
(3)

where f_0 is the water vapor mixing ratio at the peak (1 ppv), z_0 is the release altitude (85 km), and H_0 is the effective scale height of the distribution (Chamberlain, 1995). We choose a scale height of 3 km so that peak water vapor distribution provides enough water to locally cool the atmosphere down to the frost point throughout the region of the lidar cloud observations (78–92 km, Figure 9). We model the filaments as 3-m wide, centered every 5 m, and assume that each filament cools independently of the filaments above and below it. We use the largest cooling rates associated with the center of the filaments in our simulation.

Once in the ice phase, the particles warm due to the absorption of both IR terrestrial radiation and solar radiation (Espy & Jutt, 2002). We quantify the IR contribution by a simple parameterization that depends only on the equivalent water ice mixing ratios

$$\frac{dT}{dt} = 0.68 \times P_{\text{terr}} \times \mu_{\text{ice}} \tag{4}$$

where dT/dt is in K/s, P_{terr} is the heating by terrestrial IR radiation between 10 and 14 microns in W/cm³ and μ_{ice} is in ppv (Siskind et al., 2007). The constant 0.68 has units cm³/(J/K)J. We calculate the heating rates as a function of equivalent water vapor mixing ratio (Figure 10). The terrestrial heating can vary between 17 and 56 W/cm³ based on the temperature of the IR emitting surface (e.g., cloud tops at 220 K, bare ground at 283 K). We adopt the smaller value in this study based on results of a previous observational study (Siskind et al., 2007). While the Super Soaker water release occurred at night when the solar heating was zero, for completeness we also show the dependence of the heating rate due to absorption of the solar radiation of value 16 W/cm³.

Figure 11 shows the water vapor mixing ratio and cooling rates in a plume filament near the peak of the initial water vapor distribution at 85 km. The peak water vapor mixing ratios are near 1 ppv upon the release

COLLINS ET AL. 12 of 21

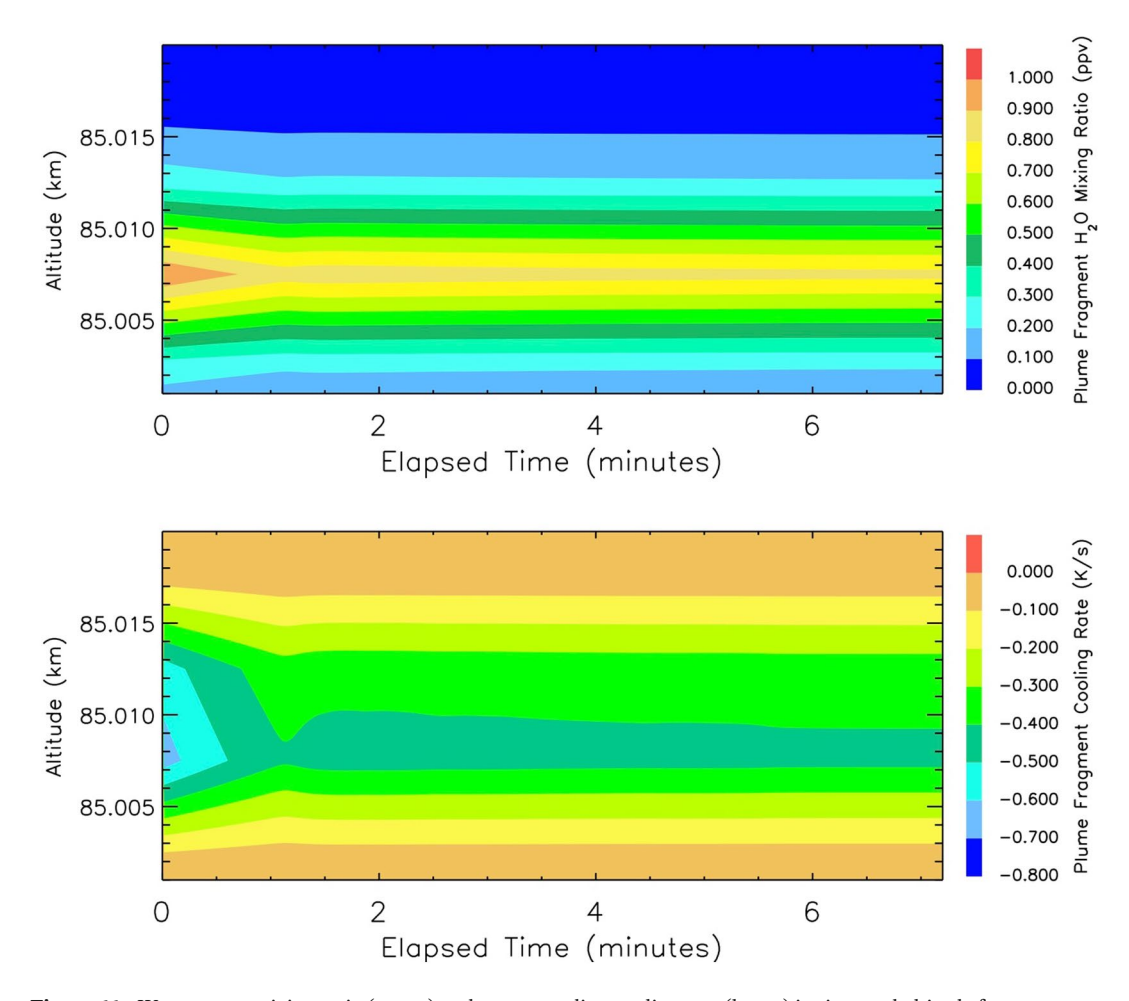


Figure 11. Water vapor mixing ratio (upper) and corresponding cooling rate (lower) in time and altitude for a water filament near the 85 km altitude of the Super Soaker water release. See text for details.

and then decrease to about 0.8 ppv during the simulation. As expected, the cooling rates are larger when water vapor mixing ratios are larger and smaller when water vapor mixing ratios are smaller. The calculated peak cooling rates are between 0.4 and 0.7 K/s. We use the cooling rate of each filament at each altitude as well as its time dependence to determine how the water vapor cooling of the expanding plume evolves with both altitude and time. This is shown in Figure 12 where we have overlaid the Rayleigh lidar observations of the cloud peak for reference. The cooling rates are highest near 85 km as expected from our initial distribution of water vapor and fall off at the top and bottom of our model domain. The extremely rapid cooling shown in the first minute leads to ice cloud formation as temperatures are quickly driven down to the elevated frost point.

Once the ice forms, heating occurs due to latent heating and absorption of terrestrial radiation (e.g., Espy & Jutt, 2002). Figure 13 shows the latent heating due to the change of phase from vapor to ice. The latent heating rate is explicitly calculated by

$$\frac{dT}{dt} = \frac{L_{\rm e} \frac{dm}{dt} n_p}{C_p \rho_a} \tag{5}$$

where dT/dt is in K/s, L_e is the latent heat of sublimation (erg/g), dm/dt is the ice particle growth rate (g/s), n_p is the particle number density (cm⁻³), ρ_a is the atmospheric density (g/cm³), and C_p is the specific heat of the atmosphere at constant pressure (erg g⁻¹ K⁻¹; Bardeen et al., 2010). The latent heating is briefly large (~0.6 K/s) and balances the large cooling from the water vapor. The IR heating from the ice particles (Equa-

COLLINS ET AL. 13 of 21

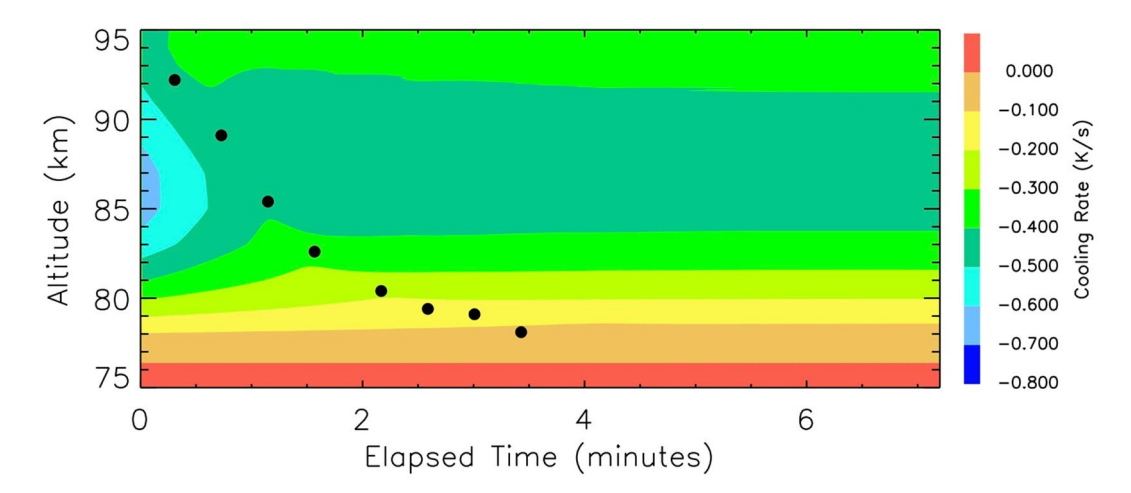


Figure 12. Water vapor cooling rate in time and altitude. The cooling rate for each 5 m layer is calculated assuming narrow filaments of water vapor. The Rayleigh lidar cloud observations are overlaid as black circles. See text for details.

tion 4) takes more time to become apparent as the ice particles need to grow large enough for the heating to become significant.

Figure 14 (upper panel) shows the time evolution of the water ice mixing ratio for the conditions of the Super Soaker experiment, where we have again overlaid the lidar cloud observations for comparison. The initial formation of ice particles agrees well with the altitude and time of the cloud observations. The onset of ice formation for any given altitude is driven by the combination of the assumed initial water vapor mixing ratio following the release (Figure 9), the length scale of the filaments (Figure 10), and the initial temperature profile (Figure 3). Figure 14 (lower panel) shows the terrestrial IR ice particle heating rate corresponding to the accompanying water ice mixing ratio. The heating rate is large when the water ice mixing ratio is large and small when the ice particle mixing ratio is small. Maximum heating values are near 0.4 K/s, much larger than the ice particle heating rates typically calculated for polar summer conditions of \sim 1 K/day (Siskind et al., 2007). This extreme heating reflects the high humidity of the release. The competition between the cooling and the heating is evident where the cooling is large when the heating is small and vice versa as the water alternates between the vapor and ice phase (Figures 12–14). Figure 15 shows the sum of the cooling rate and the two heating rates (Figures 12–14, respectively). Ultimately there is a balance between the IR cooling and IR heating with near zero net heating, due to the initial radiative cooling and the subsequent latent heating and water ice heating.

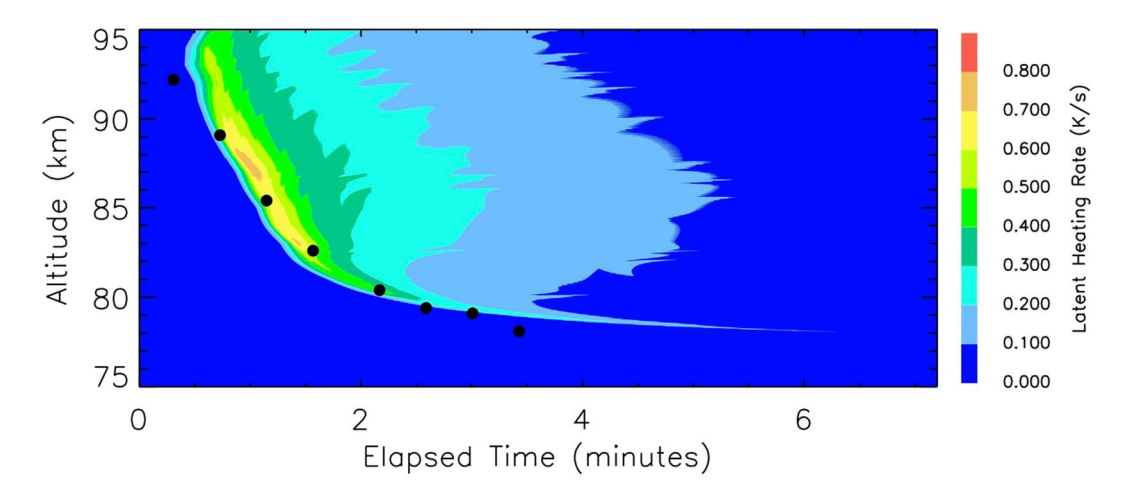


Figure 13. Latent heating resulting from ice formation after the release of water vapor at 85 km in time and altitude. The Rayleigh lidar cloud observations are overlaid as black circles. See text for details.

COLLINS ET AL. 14 of 21

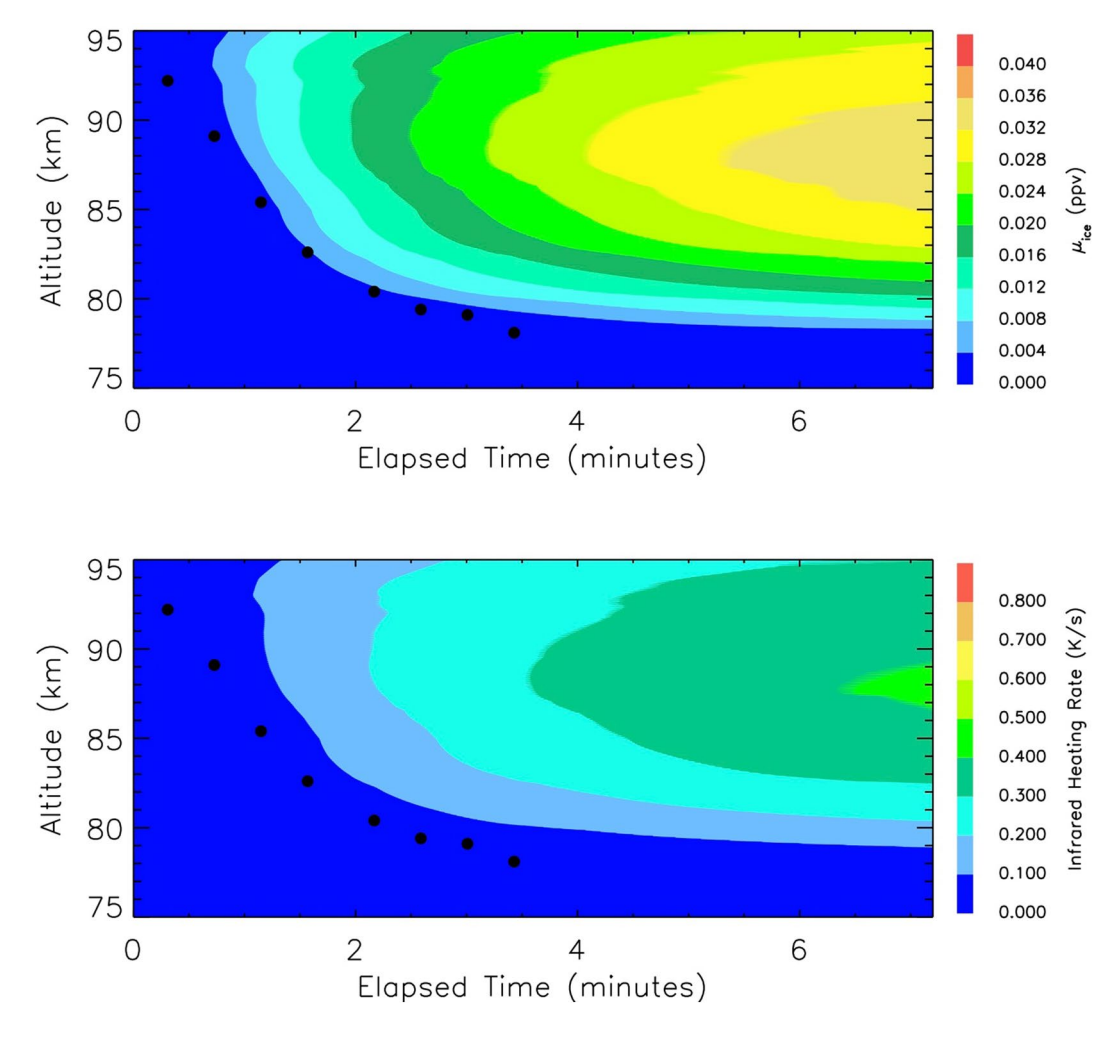


Figure 14. Equivalent water ice mixing ratio (upper and ice particle heating rate (lower) as a function of time and altitude. The Rayleigh lidar cloud observations are overlaid as black circles. See text for details.

The variation of temperature in altitude and time within the expanding plume as well as the temperature change from the initial condition are shown in Figure 16. Temperatures are near 190 K where the cloud observations are made and there is a trough of low temperatures that roughly aligns with the observations. This is the result of competition between the cooling in the vapor phase and the heating in the ice phase. As discussed earlier, the frost point temperatures for water are elevated due to the high humidity and 190 K is more than sufficient to form ice particles (Figures 8 and 11). In the region where the ice cloud is present the supersaturation with respect to ice is between 3 and 30 which is well above the value of 1 that is required for ice particles to exist.

Neither the SRWTL nor the AMTM detect (Figures 3 and 4) the simulated decrease in temperature (Figure 16). The cadence of the SRWTL measurements was 15 min, the spot size was 45 m, the profile was smoothed over 1 km in altitude, and the lidar measurement was located 24.5 km from the release. The cadence of the AMTM was 12 s, the horizontal resolution of each pixel was 0.625 km square, and the temperature is integrated through the whole OH layer (FWHM \sim 7–8 km). We conclude that the cloud formation was too rapid, the cloud structure was too fine, and the cloud motion too swift for the cooling to be directly observed by either the SRWTL or the AMTM. The cooling of the air due to the cloud is concentrated around the cloud as it expanded and we have applied the model in the rest frame of the expanding cloud. We expect that the large and recurrent releases of water due to plumes of vehicle exhaust would yield significant and more uniform cooling of the atmosphere.

COLLINS ET AL. 15 of 21

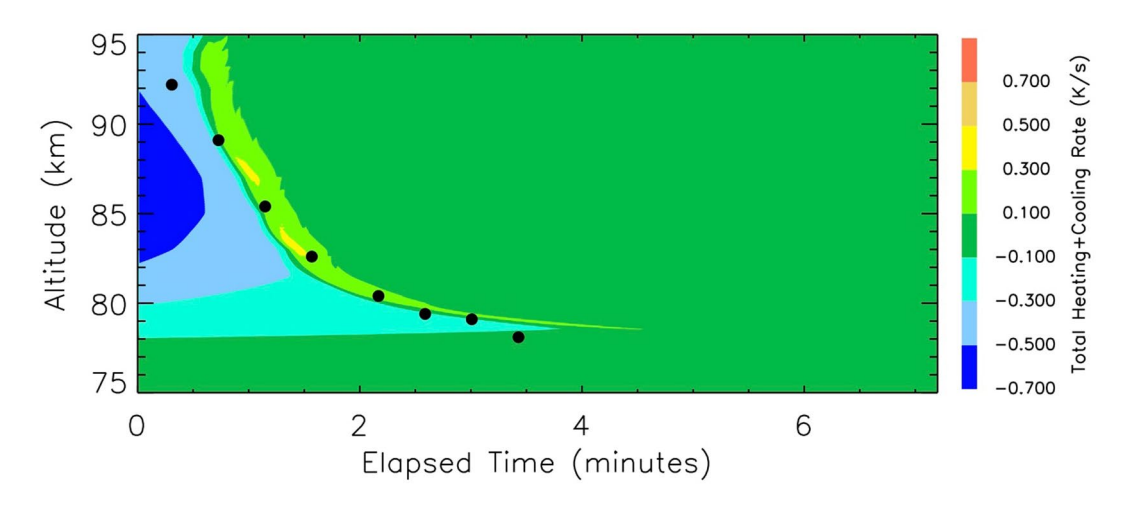


Figure 15. Total water heating rate based on vapor cooling, latent heating, and water ice heating rate as a function of time and altitude. The Rayleigh lidar cloud observations are overlaid as black circles. See text for details.

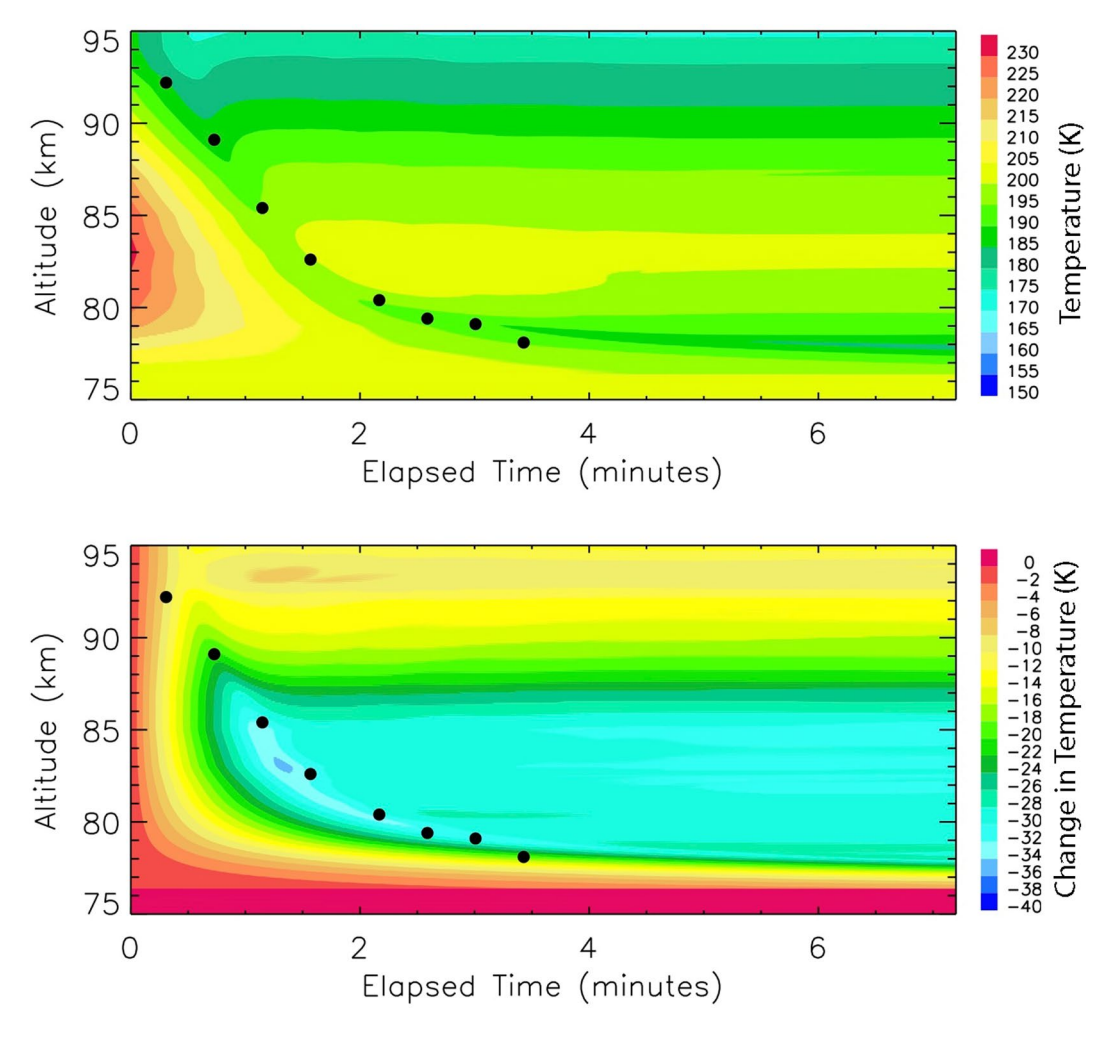


Figure 16. Upper: The evolution of temperature in the water release as a function of time and altitude. The Rayleigh lidar cloud observations are overlaid as black circles and fall in a cold trough of the model results. Lower: The difference between the initial temperature profile (Figure 3) and the temperatures in the simulation following the release of water.

COLLINS ET AL. 16 of 21

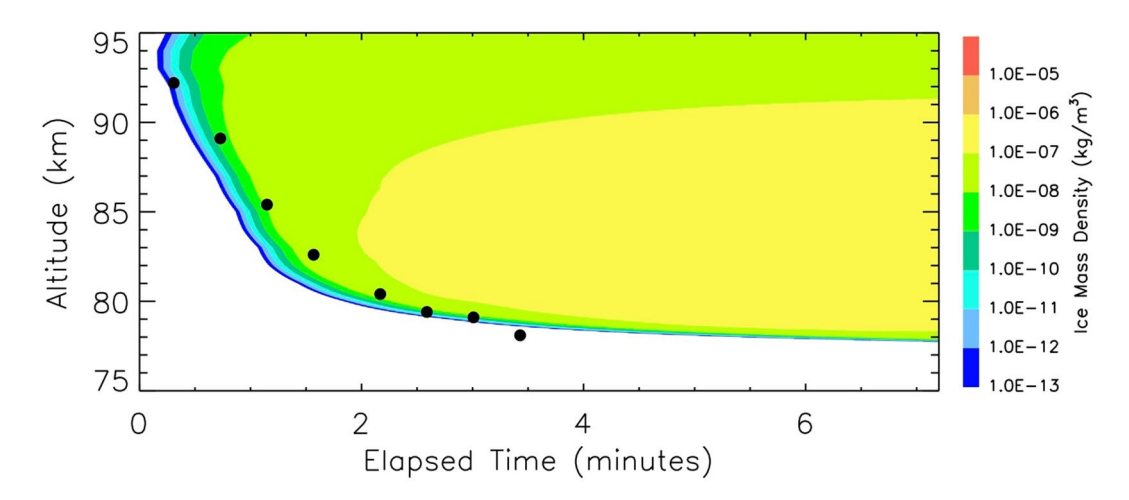


Figure 17. The ice mass density within the water release as a function of time and altitude. The Rayleigh lidar cloud observations are overlaid as black circles. See text for details.

In Figure 17, we show the ice mass density simulated by CARMA as a function of time and altitude. These model ice mass densities are several orders of magnitude greater than those estimated directly from the Rayleigh lidar observations in Section 3.2. To compare the simulation with the observations, we need to convert the model results to the lidar rest frame and then average the model results in time and altitude. Based on the arrival time of the cloud at each altitude from the water release (18-205 s), we calculate that the speed of the water from its release point to the lidar beam 3.7 km away is between 18 and 206 m/s. At the lidar beam we assume that the 220 kg of water released formed a uniform spherical shell that was 1.35 m thick. The lidar beam has a divergence of less than 0.5 mrad and a spot size of less than 45 m at 90 km. Considering the leading edge of the spherical shell cloud as a thin vertical slab, the cloud passes through the lidar beam in 0.2 s, 125 times less than the 25 s integration time of the lidar profile. However, the scattering from the air is from the entire volume of the beam while the cloud only fills a fraction (1.35/40 = 1/29.6) of the beam. Thus over a 25 s integration interval the backscatter ratio measured by the lidar is a factor of 3,700 (= 125×29.6) less than the backscatter ratio of the cloud. In the last cloud observation, the cloud echo is due to the lower edge of the shell passing overhead and the echo descends over 775 m in 25 s. In this case the backscatter ratio of the cloud measured by the lidar is a factor of 574 (= 775/1.35) less than the backscatter ratio of the cloud. The lidar estimate of the ice mass density is proportional to the backscatter ratio, and so the ice mass density of the cloud is also underestimated by the lidar.

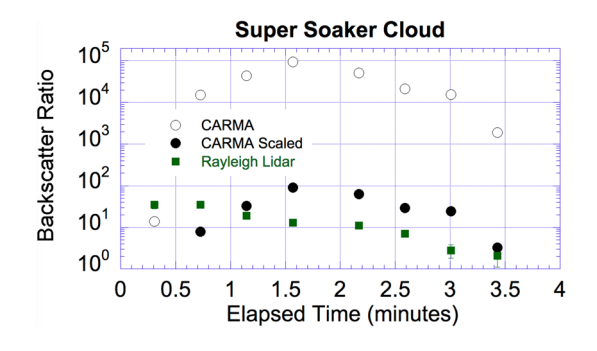


Figure 18. A comparison of the aerosol backscatter ratio derived from CARMA and the Rayleigh lidar measurements. The CARMA results are plotted as open circles. The scaled CARMA results (based on the speed and geometry of the water release) are plotted as black circles. The Rayleigh lidar measurements are plotted as green squares. CARMA, Community Aerosol and Radiation Model for Atmospheres.

We also calculate a backscatter ratio from the ice mass densities and directly compare it with the Rayleigh lidar measurements of the aerosol backscatter ratio (Table 1). The comparison is shown in Figure 18, where we have interpolated the model results onto the midpoint of each cloud timestep and averaged the model results in altitude over ±24 m to represent the vertical resolution of the lidar. We scale the ice mass densities by 3,700 for the first observation and progressively reduce the scale factor to 574 in the last observation. The model results in Figure 18 are in general agreement with the range of backscatter ratio values determined from the lidar measurements. Given the uncertainties in the vertical and horizontal distribution of the water vapor, this level of agreement between the data and model is significant. More importantly, the observed altitude and onset of cloud formation is largely reproduced by the model (Figure 17). CARMA also calculates the ice particle radii produced in the exotic, water rich environment of the Super Soaker experiment. Early in the simulation ice particle radii are calculated to be between 10 and 100 nm, whereas later in the simulation the radii can exceed 300 nm. These particles have sedimentation speeds that are much lower than the

COLLINS ET AL. 17 of 21



observed descent rate of the cloud. Quantitative analysis of the ice particle sizes is sensitive to the water vapor distribution, which we can only estimate in our experiment. However, we emphasize that the onset of ice formation in both time and altitude is reproduced in our simulation under inhospitable conditions for mesospheric cloud formation due to the quantitative consideration of IR cooling by narrow concentrated water vapor filaments.

6. Discussion and Conclusions

We have presented an observational and modeling study of a cloud resulting from a water release in the upper mesosphere. We observed this mesospheric cloud 18 s after the explosive release of 220 kg of water at 85 km. We have analyzed this cloud under the assumption that it is composed of water ice. By adding IR water vapor cooling to the microphysical model, we have reproduced the altitude and the onset of ice cloud formation observed by our ground-based Rayleigh lidar in the winter mesosphere where ice clouds are rarely observed. The model results show that the cloud forms due to the combined effects of rapid IR cooling (\sim 25 K) by meter-scale filaments of nearly pure water vapor (\sim 1 ppv) and an increase in frost point (\sim 50 K from \sim 150–200 K) due to this high humidity. Following the formation of the ice cloud, the model results indicate that latent heating and IR heating by the ice particles together balance the water vapor cooling. The result of this balance of cooling in the vapor phase and heating in the ice phase is that the water acts as a thermostat to maintain the local temperature near the frost point. This scenario is consistent with the fact that the lower edge of naturally occurring PMCs are found at temperatures that are remarkably repeatable of 150 K near 82 km (Lübken et al., 1996).

The Super Soaker cloud forms so rapidly that we do not expect variations in the condensation nuclei and eddy diffusion to significantly affect the cloud development. Modifications to the condensation nuclei and to the eddy diffusion profiles in the model could alter the calculated ice particle characteristics but a sensitivity study involving variations to these inputs and the resultant impact on the cloud characteristics is beyond the scope of the current study. This is primarily due to the limited number of observations available to constrain such a study and our limited knowledge of the vertical and horizontal distribution of the water vapor following its explosive release.

The small filaments of water vapor simulated here cannot be resolved by satellite-borne instruments and thus models constrained by direct satellite observations of water vapor cannot address the microphysics at these meter-scales directly. The limb viewing satellite instruments assume spherical symmetry over length scales of hundreds of kilometers that are a factor of 10^5 larger than studied here. Recent balloon-borne imager observations have revealed structures as small as 30 m in PMCs (Fritts et al., 2017). Regardless of the length scale of an upper mesospheric water vapor parcel, local mixing ratios of 10 ppmv or more create cooling in excess of 10 K/day (Figure 10), which can dominate the energetics of the upper mesosphere (Fomichev et al., 2004; Thomas, 1996; Zhu, 1994). Additional insight to what controls the energetics of the upper mesosphere in the presence of water ice clouds could be gained with simultaneous observations of mesospheric clouds, water vapor, and temperatures. This would require measurements of water vapor and temperatures at significantly higher spatial (meters) and temporal (seconds) resolution than currently possible.

In the presence of pure, or nearly pure, water vapor the water frost point temperature in the upper mesosphere is near 200 K (Figure 9). This is about 50 K higher than the water frost point when water vapor mixing ratios are at the typical values of a few ppmv in the polar summer mesosphere. This effect was previously demonstrated in a study of satellite observations of the Space Shuttle main engine plume, which is almost entirely water vapor (Stevens et al., 2002). In that study, OH dayglow observations and water ice were observed simultaneously in the upper mesosphere under conditions normally inhospitable to cloud formation. The OH dayglow observations were a proxy for water vapor in the upper mesosphere. Our conclusion from the Super Soaker experiment that high concentrations of water vapor actively cool the upper mesosphere and drive the temperature down to the elevated frost point confirms these earlier observations of simultaneously observed OH and water ice.

Water vapor is a common effluent in space traffic exhaust. Previous work has shown that the space shuttle main engine plume provided a reservoir of water in the upper atmosphere that produced bursts of

COLLINS ET AL. 18 of 21



mesospheric cloudiness following launch. This was observed in the Arctic summer (Collins et al., 2009; Kelley et al., 2010; Stevens, Englert et al., 2005a; Stevens et al., 2003; Stevens et al., 2012), at high northern latitudes in the fall (Stevens et al., 2002), and in the Antarctic summer (Stevens, Meier, et al., 2005b). The summer polar mesosphere is distinguished by vigorous and persistent vertical upwelling (e.g., Berger & von Zahn, 2002). The introduction of concentrated filaments of water vapor leading to the formation of mesospheric ice clouds as described herein would have more persistent effects in the summer, as the vertical winds could sustain the ice particles in the upper mesosphere where they could be observed repeatedly. This might explain why the formation of mesospheric clouds by space traffic is more readily observed in the summer than in the winter. Nonetheless, while space traffic water exhaust serves as a reservoir for mesospheric cloud production, this study suggests that the exhaust can also actively cool the mesosphere and induces the formation of mesospheric clouds, even in the polar winter.

Data Availability Statement

The data presented in this study are available at NASA's publication repository, NASA PubSpace (https://www.ncbi.nlm.nih.gov/pmc/funder/nasa/).

Acknowledgments

The authors acknowledge the National Aeronautics and Space Administration (NASA) staff, the NASA Sounding Rockets Operations Contractor staff at Wallops Flight Facility, and the University of Alaska Fairbanks (UAF) staff at Poker Flat Research Range for their support of the Super Soaker experiment. The authors thank Jay Scott who was the Super Soaker mission manager. The authors thank Gang Chen and Mohammad Hoveidafar of UAF for conducting a survey of the lidar site and assisting in the orientation of the Rayleigh lidar telescope, and Mikayla Grunin for assisting in the optical alignment of the steerable Rayleigh lidar telescope. The authors thank Pattilyn McLaughlin and Vanessa Chambers of Utah State University (USU) for assistance in operating the USU cameras. The authors also thank Henrike Wilms of the German Aerospace Center for providing the initial version of the CARMA model used in this study. The authors thank Xinzhao Chu and two other anonymous reviewers for their critical reviews. The steerable lidar telescope was originally donated to UAF by the National Institute of Information and Communications Technology, Japan. The Super Soaker experiment was funded by the NASA Heliophysics Division under grant NNX16AF67G to ASTRA with subcontracts to Clemson University, UAF, and USU and grant NNG17WF02I to the Naval Research Laboratory. The resonance lidar observations were conducted and analyzed with support from the National Science Foundation under grants AGS-1552214, AGS-1734852, AGS-1734693, and AGS-1829138. PFRR is a rocket range operated by the UAF Geophysical Institute with support from NASA.

References

Akhavan, J. (1998). The chemistry of explosives. Cambridge: The Royal Society of Chemistry.

Bardeen, C. G., Toon, O. B., Jensen, E. J., Hervig, M. E., Randall, C. E., Benze, S., et al. (2010). Numerical simulations of the three-dimensional distribution of polar mesospheric clouds and comparisons with Cloud Imaging and Particle Size (CIPS) experiment and the Solar Occultation For Ice Experiment (SOFIE) observations. *Journal of Geophysical Research*, 115, D10204. https://doi.org/10.1029/2009JD012451

Berger, U., & von Zahn, U. (2002). Icy particles in the summer mesopause region: Three-dimensional modeling of their environment and two-dimensional modeling of their transport. *Journal of Geophysical Research*, 107(A11), 1366. https://doi.org/10.1029/2001JA000316

Bills, R. E., Gardner, C. S., & Franke, S. J. (1991). Na Doppler/temperature lidar: Initial mesopause region observations and comparison with the Urbana medium frequency radar. *Journal of Geophysical Research*, 96, 22701–22707. https://doi.org/10.1029/91JD02206

Bohren, C. F., & Huffman, D. R. (1983). Absorption and scattering of light by small particles. (pp 544). New York, NY: Wiley.

Cai, X., Yuan, T., Zhao, Y., Pautet, P. D., Taylor, M. J., & Pendleton, W. R., Jr (2014). A coordinated investigation of the gravity wave breaking and the associated dynamical instability by a Na lidar and an advanced mesosphere temperature mapper over Logan, UT (41.7°N, 111.8°W). *Journal of Geophysical Research: Space Physics*, 119, 6852–6864. https://doi.org/10.1002/2014JA020131

Chamberlain, J. W. (1995). Physics of the aurora and airglow. Washington, DC: American Geophysical Union.

Chen, C., Chu, X., Zhao, J., Roberts, B. R., Yu, Z., Fong, W., et al. (2016). Lidar observations of persistent gravity waves with periods of 3–10 h in the Antarctic middle and upper atmosphere at McMurdo (77.83°S, 166.67°E). *Journal of Geophysical Research: Space Physics*, 121, 1483–1502. https://doi.org/10.1002/2015ja022127

Chu, X., Huang, W., Fong, W., Yu, Z., Wang, Z., Smith, J. A., et al. (2011). First lidar observations of polar mesospheric clouds and Fe temperatures at McMurdo (77.8°S,166.7°E), Antarctica. *Geophysical Research Letters*, 38(16), L16810. https://doi.org/10.1029/2011gl048373 Collins, R. L., Lehmacher, G. A., Larsen, M. F., & Mizutani, K. (2011). Estimates of vertical eddy diffusivity in the upper mesosphere in the presence of a mesospheric inversion layer. *Annales Geophysicae*, 29, 2019–2029. https://doi.org/10.5194/angeo-29-2019-2011

Collins, R. L., Taylor, M. J., Neilson, K., Mizutani, K., Murayama, Y., Sakanoi, K., et al. (2009). Noctilucent cloud in the Western Arctic in 2005: Simultaneous lidar and camera observations and analysis. *Journal of Atmospheric and Solar-Terrestrial Physics*, 71, 446–452. https://doi.org/10.1016/j.jastp.2008.09.044

DeLand, M. T., & Thomas, G. E. (2019). Evaluation of space traffic effects in SBUV polar mesospheric cloud data. *Journal of Geophysical Research: Atmospheres*, 124, 4203–4221. https://doi.org/10.1029/2018JD029756

Espy, P. J., & Jutt, H. (2002). Equilibrium temperature of water-ice aerosols in the high-latitude summer mesosphere. *Journal of Atmospheric and Solar-Terrestrial Physics*, 64, 1823–1832.

Fiedler, J., Baumgarten, G., & von Cossart, G. (2003). Noctilucent clouds above ALOMAR between 1997 and 2001: Occurrence and properties. *Journal of Geophysical Research*, 108(D8), 8453. https://doi.org/10.1029/2002JD002419

Flatau, P. J. (2018). BHMIE.PRO: A Bohren-Huffman Mie scattering subroutine to calculate scattering and absorption by a homogenous isotropic sphere. http://scatterlib.wikidot.com/mie

 $Fomichev, V.I., Fu, C., de \ Grandpr\'e, J., \ Beagley, S.\ R., \ Ogibalov, V.\ P., \& \ McConnell, J.\ C.\ (2004). \ Model \ thermal\ response to \ minor\ radiative energy sources and sinks in the middle atmosphere. \ \textit{Journal of Geophysical Research}, 109, D19107. \ https://doi.org/10.1029/2004JD004892$

Fricke, K.-H., Müller, K. P., Langer, M., Römke, K., & Lübken, F. J. (1996). Visual and lidar observation of rocket induced effects in the upper atmosphere above Andøya on January 25, 1995. *Proceedings of the 12th ESA Symposium on European Rocket and Balloon Programmes and Related Research, Lillehammer, Norway.* (pp. 107–112). Neuilly, France: Eur. Space Agency (ESA SP-370).

Fritts, D. C., Wang, L., Baumgarten, G., Miller, A. D., Geller, M. A., Jones, G., et al. (2017). High-resolution observations and modeling of turbulence sources, structures, and intensities in the upper mesosphere. *Journal of Atmospheric and Solar-Terrestrial Physics*, 162, 57–78. https://doi.org/10.1016/j.jastp.2016.11.006

 $Gadsden,\,M.\,\,(1982).\,\,Noctilucent\,\,clouds.\,\,Space\,\,Science\,\,Reviews,\,33,\,279-334.$

Heale, C. J., Bossert, K., Snively, J. B., Frits, D. C., Pautet, P. D., & Taylor, M. J. (2017). Numerical modeling of a multiscale gravity wave event and its airglow signatures over Mount Cook, New Zealand, during the DEEPWAVE campaign. *Journal of Geophysical Research:* Atmospheres, 122, 846–860. https://doi.org/10.1002/2016JD025700

Hedin, A. E. (1991). Extension of the MSIS thermosphere model into the middle and lower atmosphere. *Journal of Geophysical Research*, 96(A2), 1159–1172. https://doi.org/10.1029/90JA02125

Houghton, J. T. (2002). The physics of atmospheres (3rd ed., pp. 320). New York, NY: Cambridge University Press.

COLLINS ET AL. 19 of 21



- Jensen, E., & Thomas, G. E. (1988). A growth-sedimentation model of polar mesospheric clouds: Comparison with SMR measurements. Journal of Geophysical Research, 93, 2461–2473. https://doi.org/10.1029/JD093iD03p02461
- Kelley, M.C., Nicolls, M. J., Varney, R. H., Collins, R. L., Doe, R., & Plane, J. M. C. (2010). Radar, lidar, and optical observations in the polar summer mesosphere shortly after a space shuttle launch. *Journal of Geophysical Research*, 115, A05304. https://doi. org/10.1029/2009JA014938
- Krueger, D. A., She, C. Y., & Yuan, T. (2015). Retrieving menopause temperature and line-of-sight wind from full-diurnal cycle Na lidar observations. *Applied Optics*, 54, 9469–9488.
- Li, J. (2019). Lidar and radar studies of turbulence, instabilities, and waves in the Arctic middle atmosphere. (pp. 242). (PhD Dissertation). Fairbanks, AK: University of Alaska Fairbanks.
- Li, J., Williams, B. P., Alspach, J. H., & Collins, R. L. (2020). Sodium resonance wind-temperature lidar at PFRR: Initial observations and performance. *Atmosphere*, 11, 98. https://doi.org/10.3390/atmos11010098
- Liu, H. L. (2007). On the large wind shear and fast meridional transport above the mesopause. *Geophysical Research Letters*, 34, L08815. https://doi.org/10.1029/2006GL028789
- Lübken, F. J., Fricke, K. H., & Langer, M. (1996). Noctilucent clouds and the thermal structure near the Arctic mesopause in summer. Journal of Geophysical Research, 101(D5), 9489–9508. https://doi.org/10.1029/96JD00444
- Marsh, D. R., Smith, A. K., Mlynczak, M. G., & Russell, J. M. (2006). SABER observations of the OH Meinel airglow variability near the mesopause. *Journal of Geophysical Research*, 111, A10. https://doi.org/10.1029/2005JA011451
- Marti, J., & Mauersberger, K. (1993). A survey and new measurements of ice vapor pressure at temperatures between 170 and 250 K. Geo-physical Research Letters, 20, 363–366. https://doi.org/10.1029/93GL00105
- Measures, R. M. (1992). Laser remote sensing: Fundamentals and applications. (pp. 523). Malabar: Kreiger.
- Meier, R. R., Plane, J. M., Stevens, M. H., Paxton, L. J., Christensen, A. B., & Crowley, G. (2010). Can molecular diffusion explain Space Shuttle plume spreading? *Geophysical Research Letters*, 37, L08101. https://doi.org/10.1029/2010GL042868
- Meriwether, J. W. (1975). High latitude airglow observations of correlated short-term fluctuations in the hydroxyl meinel 8-3 band intensity and rotational temperature. *Planetary and Space Science*, 23, 1211–1221. https://doi.org/10.1016/0032-0633(75)90170-1
- Mesquita, R. L. A., Larsen, M. F., Azeem, I., Stevens, M. H., Williams, B. P., Collins, R. L., et al. (2020). In situ observations of neutral shear instability in the statically stable high-latitude mesosphere and lower thermosphere during quiet geomagnetic conditions. *Journal of Geophysical Research: Space Physics*, 125, e2020JA027972. https://doi.org/10.1029/2020JA027972
- Pautet, P.-D., Taylor, M. J., Pendleton, W. R., Zhao, Y., Yuan, T., Esplin, R., et al. (2014). An advanced mesospheric temperature mapper for high-latitude airglow studies. *Applied Optics*, 53(26), 5934–5943.
- Pautet, P. D., Taylor, M. J., Snively, J. B., & Solorio, C. (2018), Unexpected occurrence of mesospheric frontal gravity wave events over South Pole (90°S), Journal of Geophysical Research: Atmospheres, 123, 160–173. https://doi.org/10.1002/2017JD027046
- Picone, J. M., Hedin, A. E., Drop, D. P., & Aikin, A. C. (2002). NRLMSISE-00 empirical model of the atmosphere: Statistical comparisons and scientific issues. *Journal of Geophysical Research*, 107, 1468. https://doi.org/10.1029/2002JA009430
- Pumphrey, H. C., Lambert, A., & Livesey, N. J. (2011). Observation of the exhaust plume from the space shuttle main engines using the microwave limb sounder. *Atmospheric Measurement Techniques*, 4, 89–95.
- Rapp, M., & Thomas, G. E. (2006). Modeling the microphysics of mesospheric ice particles: Assessment of current capabilities and basic sensitivities. *Journal of Atmospheric and Solar-Terrestrial Physics*, 68, 715–744.
- Reid, G. C. (1975). Ice clouds at the summer polar mesopause. Journal of the Atmospheric Sciences, 32, 523-535.
- Roble, R. G., & Ridley, E. C. (1994). A Thermosphere-Ionosphere-Mesosphere-Electrodynamics General Circulation model (TIME-GCM): Equinox solar cycle minimum simulation (30–500 km). Geophysical Research Letters, 21, 417–420. https://doi.org/10.1029/93GL03391
- Russell, J. M., III, et al. (2009). The Aeronomy of Ice in the Mesosphere (AIM) mission: Overview and early science results. *Journal of Atmospheric and Solar-Terrestrial Physics*, 71, 289–299.
- She, C. Y., Latifi, H., Yu, J. R., Alvarez, R. J., II, Bills, R. E., & Gardner, C. S. (1990). Two-frequency lidar technique for mesospheric Na temperature measurements. *Geophysical Research Letters*, 17, 929–932.
- Siskind, D. E., Hervig, M., Gumbel, J., & Stevens, M. H. (2007). Polar mesospheric cloud mass and the ice budget: 3. Application of a coupled ice-chemistry-dynamics model and comparison with observations. *Journal of Geophysical Research*, 112, D08303. https://doi.org/10.1029/2006JD007499
- Siskind, D. E., Stevens, M. H., Hervig, M. E., & Randall, C. E. (2013). Recent observations of high mass density polar mesospheric clouds: A link to space traffic? *Geophysical Research Letters*, 40, 2813–2817. https://doi.org/10.1002/grl.50540
- Stevens, M. H., Englert, C. R., DeLand, M. T., & Hervig, M. (2005a). The polar mesospheric cloud mass in the Arctic summer. *Journal of Geophysical Research*, 110, A02306. https://doi.org/10.1029/2004JA010566
- Stevens, M. H., Englert, C. E., & Gumbel, J. (2002). OH observations of space shuttle exhaust. *Geophysical Research Letters*, 29, 5. https://doi.org/10.1029/2002GL015079
- Stevens, M. H., Gumbel, J., Englert, C. R., Grossmann, K. U., Rapp, M., & Hartogh, P. (2003). Polar mesospheric clouds formed from space shuttle exhaust. *Geophysical Research Letters*, 30, 1546. https://doi.org/10.1029/2003GL017249
- Stevens, M. H., Lossow, S., Fiedler, J., Baumgarten, G., Lübken, F. J., Hallgren, K., et al. (2012). Bright polar mesospheric clouds formed by main engine exhaust from the space shuttle's final launch. *Journal of Geophysical Research*, 117, D19206. https://doi.org/10.1029/2012JD017638
- Stevens, M. H., Lossow, S., Siskind, D. E., Meier, R. R., Randall, C. E., Russell, J. M., III, et al. (2014). Space shuttle exhaust plumes in the lower thermosphere: Advective transport and diffusive spreading. *Journal of Atmospheric and Solar-Terrestrial Physics*, 108, 50–60.
- Stevens, M. H., Meier, R. R., Chu, X., DeLand, M. T., & Plane, J. M. C. (2005b). Antarctic mesospheric clouds formed from space shuttle exhaust. *Geophysical Research Letters*, 32, L13810. https://doi.org/10.1029/2005GL023054
- Thomas, G. E. (1996). Global change in the mesosphere-lower thermosphere region: has it already arrived? *Journal of Atmospheric and Terrestrial Physics*, 58, 1629–1656.
- Thurairajah, B. (2009). Role of waves on the circulation of the Arctic middle atmosphere: Rayleigh lidar measurements and analysis. (pp. 182). (PhD Dissertation). Fairbanks, AS: University of Alaska Fairbanks.
- von Savigny, C., & Burrows, J. P. (2007). Latitudinal variation of NLC particle radii derived from northern hemisphere SCIAMACHY/ Envisay limb measurements. *Advances in Space Research*, 40, 765–771.
- von Zahn, U., & Berger, U. (2003). Persistent ice cloud in the midsummer upper mesosphere at high latitudes: Three-dimensional modeling and cloud interactions with ambient water vapor. *Journal of Geophysical Research*, 108, 8451. https://doi.org/10.1029/2002JD002409
- Warren, S. G., Thomas, G. E., Hernandez, G., & Smith, R. W. (1997). Noctilucent cloud observed in late April at South Pole Station: Temperature anomaly or meteoritic debris? *Journal of Geophysical Research*, 102(D2), 1991–2000. https://doi.org/10.1029/96JD02513

COLLINS ET AL. 20 of 21



- Wilms, H., Rapp, M., & Kirsch, A. (2016). Nucleation of mesospheric cloud particles: Sensitivities and limits. *Journal of Geophysical Research: Space Physics*, 121, 2621–2644. https://doi.org/10.1002/2015JA021764
- Woodbridge, D. D., Lasater, J. A., Fultz, B. M., Clark, R. E., & Wylie, N. (1963). An analysis of the second project high water data. NASA CR-158553, REPT-02.01 19790078055.
- Woodbridge, D. D., & Lasater, J. A. (1965). An analysis of project high water data. NASA Report Number: NASA-CR-57946, Document ID: 19650011729.
- Yuan, T., Heale, C. J., Snively, J. B., Cai, X., Pautet, P. D., Fish, C., et al. (2016). Evidence of dispersion and refraction of a spectrally broad gravity wave packet in the mesopause region observed by the Na lidar and mesospheric temperature mapper above Logan, Utah. *Journal of Geophysical Research: Atmospheres*, 121, 579–594. https://doi.org/10.1002/2015JD023685
- Yuan, T., Pautet, P. D., Zhao, Y., Cai, X., Criddle, N. R., Taylor, M. J., et al. (2014). Coordinated investigation of midlatitude upper mesospheric temperature inversion layers and the associated gravity wave forcing by Na lidar and advanced mesospheric temperature mapper in Logan, Utah. *Journal of Geophysical Research: Atmospheres*, 119, 3756–3769. https://doi.org/10.1002/2013JD020586
- Yue, J., Liu, H. L., Meier, R. R., Chang, L., Gu, S. Y., & Russell, J. (2013). On the fast zonal transport of the STS-121 space shuttle exhaust plume in the lower thermosphere. *Journal of Atmospheric and Solar-Terrestrial Physics*, 94, 19–27.
- Zhang, J., Kessler, D. J., Matney, M. J., Eichler, P., Reynolds, R. C., Anz-Meador, P. D., et al. (1997). The NASA engineering model: A new approach. *Advances in Space Research*, 19, 281–290. https://doi.org/10.1016/S0273-1177(97)00013-6
- Zhu, X. (1994). An accurate and efficient radiation algorithm for middle atmosphere models. *Journal of the Atmospheric Sciences*, 51, 3593–3614.
- Zhu, X. (2004). Radiative transfer in the middle atmosphere and planetary atmospheres. In X. Zhu, Li, M. Cai, S. Zhou, Y. Zhu, F.-F. Jin, X. Zou, & M. Zhang (Eds.) *Observation, Theory and Modeling of Atmospheric Variability* (pp. 359–396). Singapore: World Scientific Publishing Company. https://doi.org/10.1142/5431

COLLINS ET AL. 21 of 21